

Major reorganization of chromosome conformation during muscle development in pig

Maria Marti-Marimon^{1,†}, Nathalie Vialaneix², Yvette Lahbib-Mansais¹,
Matthias Zytnecki², Sylvie Camut¹, David Robelin¹, Martine Yerle-Bouissou¹
and Sylvain Foissac^{1,*}

¹ GenPhySE, Université de Toulouse, INRAE, ENVT, Castanet Tolosan, France

² Université de Toulouse, INRAE, UR MIAT, Castanet-Tolosan, France

Correspondence*:

GenPhySE, INRAE Toulouse, CS 52627, F-31326, Castanet Tolosan cedex, France
sylvain.foissac@inrae.fr

2 [†] Current affiliation: CNAG-CRG, Centre for Genomic Regulation (CRG), Barcelona Institute of Science
3 and Technology (BIST), Baldiri i Reixac 4, 08028 Barcelona, Spain

4 ABSTRACT

5 The spatial organization of the genome in the nucleus plays a crucial role in eukaryotic cell
6 functions, yet little is known about chromatin structure variations during late fetal development
7 in mammals. We performed *in situ* high-throughput chromosome conformation capture (Hi-
8 C) sequencing of DNA from muscle samples of pig fetuses at two late stages of gestation.
9 Comparative analysis of the resulting Hi-C interaction matrices between both groups showed
10 widespread differences of different types. First, we discovered a complex landscape of stable and
11 group-specific Topologically Associating Domains (TADs). Investigating the nuclear partition of the
12 chromatin into transcriptionally active and inactive compartments, we observed a genome-wide
13 fragmentation of these compartments between 90 and 110 days of gestation. Also, we identified
14 and characterized the distribution of differential *cis*- and *trans*- pairwise interactions. In particular,
15 *trans*-interactions at chromosome extremities revealed a mechanism of telomere clustering further
16 confirmed by 3D Fluorescence *in situ* Hybridization (FISH). Altogether, we report major variations
17 of the three-dimensional genome conformation during muscle development in pig, involving
18 several levels of chromatin remodeling and structural regulation.

19 **Keywords:** Hi-C, chromosome conformation, 3D genome, chromatin structure, telomeres, fetal muscle, pig, development

1 INTRODUCTION

20 Deciphering the mechanisms that govern gene expression regulation is essential for understanding the
21 fundamental biological changes occurring under different physiological conditions. In this context, genome
22 organization has been proven to be a major player in the regulation of gene expression (Bonev and Cavalli,
23 2016; Bonora et al., 2014; Long et al., 2016). Understanding the relationship between genome organization
24 and gene expression needs a deep knowledge of chromatin structure and folding, which has been made
25 possible by the development of three-dimensional (3D) techniques like 3D DNA Fluorescence *in situ*
26 Hybridization (FISH) and Chromosome Conformation Capture assays (Davies et al., 2017; Dekker et al.,

27 2002), including its genome-wide version Hi-C (Lieberman-Aiden et al., 2009). By identifying pairs of
28 genomic regions in direct physical contact or in close spatial proximity within the nucleus, hereafter referred
29 as “interactions”, these approaches revealed several features of the genome architecture. For instance,
30 individual chromosomes occupy discrete territories in the interphase nuclei, the so-called chromosome
31 territories (Cremer and Cremer, 2001; Bolzer et al., 2005; Cremer et al., 2006), which may intermingle at
32 the interface regions allowing *trans*-chromosomal interactions (Branco and Pombo, 2006; Nagano et al.,
33 2013). Moreover, chromosomes have been found to be organized in two main types of large regions with
34 different features in terms of genome topology, chromatin state and gene expression. These regions of
35 several megabases are the A and B compartments that correspond respectively to open transcriptionally
36 active and close inactive chromatin. While A compartments are associated with euchromatic, gene-rich and
37 DNase I hypersensitive regions, B compartments are considered as transcriptionally inert, heterochromatic,
38 nuclear lamina-associated, gene-poor and DNase I insensitive (Bonora et al., 2014; Gibcus and Dekker,
39 2013; Lieberman-Aiden et al., 2009). Although these compartments could be further segmented considering
40 finer epigenetics features (Rao et al., 2014) or associated with exceptional euchromatin/heterochromatin
41 organisations (Feodorova et al., 2020), we will simply refer to the general A/B definition hereinafter. At a
42 smaller scale, genomic regions of about 1 Mb with a high density of *cis*-interactions, named topologically
43 associated domains (TADs) (Dixon et al., 2012; Nora et al., 2012; Sexton et al., 2012) have been shown to
44 play a role in regulating gene expression during key biological processes like development (Gibcus and
45 Dekker, 2013; Lupiáñez et al., 2015).

46 To gain insight into the establishment, the dynamics and the function of these genomic structures, several
47 studies have characterized them in various cell types and compared them within or, sometimes, between
48 species (Dixon et al., 2012; Rudan et al., 2015; Foissac et al., 2019). Various comparisons have been
49 performed during early embryo development (Zheng and Xie, 2019), between different cell lines (*e.g.*,
50 embryonic and mesenchymal stem cells Dixon et al. (2015)), from distinct differentiation states (*e.g.*,
51 during neural differentiation Bonev et al. (2017), or during B cell fate commitment Boya et al. (2017);
52 Lin et al. (2012)). Such comparisons efficiently revealed strong differences between distinct cell types,
53 requiring few biological replicates (often simple duplicates), but they did not provide information about
54 the heterogeneity and the dynamics of the genome 3D structure for a specific cell type. The development
55 of single-cell Hi-C (Nagano et al., 2013) made possible to determine whole genome structures in single
56 haploid (Stevens et al., 2017) or diploid cells (Tan et al., 2018). Recent applications of single-cell Hi-C
57 revealed various degrees of heterogeneity in genome 3D conformation among several cell lines (Finn et al.,
58 2019; Ramani et al., 2017).

59 Despite all these efforts, little is known about the status and the dynamics of chromosome organization
60 in animal cells from most of the organized tissue types, with notable exceptions like brain and liver for
61 instance (Foissac et al., 2019; Harewood et al., 2017; Vietri Rudan et al., 2015; Won et al., 2016). Regarding
62 skeletal muscle, Hi-C experiments have been performed on cultured cells (Doynova et al., 2017; He et al.,
63 2018) and on adult muscle (Schmitt et al., 2016), but little is known about chromosome organization in
64 this type of differentiated cells during late development. To assess whether significant structural dynamic
65 modifications could also be detected there, we characterized the 3D genome organization of porcine
66 *longissimus dorsi* muscle cells during late fetal development (days 90 and 110 of gestation) by adapting
67 the *in situ* Hi-C protocol (Rao et al., 2014) to fetal frozen tissues. This period, which covers almost
68 the entire last month of gestation, is known to be crucial for porcine muscle development and maturity,
69 involving major reorganizations of the transcriptomic and proteomic programs (Voillet et al., 2014, 2018).
70 By performing the experimental assays on tissue samples from different fetuses (three replicates per group
71 of the Large White breed), we characterized the genomic structure of pig muscle cells at various levels of

72 organization, providing high-resolution Hi-C interaction maps, TAD and A/B compartment annotations.
73 Comparing samples from 90 vs. 110 days of gestation allowed the identification of major topological
74 differences between the two groups, in line with previous results from transcriptome characterization. In
75 addition, these results completed and further expanded previous studies which identified *trans* interactions
76 involving genes that are key players for fetal muscle growth and development (Lahbib-Mansais et al., 2016;
77 Marti-Marimon et al., 2018). Overall, this study sheds a new light on the description of dynamic changes of
78 the 3D genome occurring during transcriptional switches in the expression programs of differentiated cells.

2 RESULTS

79 2.1 Genome-wide maps of chromosomal interactions in fetal porcine muscle tissue

80 We produced and sequenced Hi-C libraries from muscle samples of six pig fetuses (Supplementary
81 Table 1): three replicates at 90 days of gestation (“d90” group) and three replicates at 110 days of gestation
82 (“d110” group). We obtained ~7 billion reads in total across the six samples. After trimming the sequences
83 when needed, we could map from 63 to 73% of the pairs on the *Sus scrofa* v11.1 reference genome
84 (Supplementary Table 2). These proportions are lower than usually reported with human or mouse cells
85 (Rao et al., 2014). This could be explained by several reasons, including the slightly lower quality of the
86 porcine genomic sequence compared with the human or murine ones, and the nature of the biological
87 material used here (frozen samples of fetal muscle). In each library, nevertheless, most of the mapped pairs
88 showed consistent mapping configurations with respect to the genomic positions of the HindIII restriction
89 sites (Yaffe and Tanay, 2011). Those were labeled as “valid interactions” (Supplementary Table 2). Overall,
90 we obtained between 112 M and 260 M valid interactions per sample from which we generated six
91 individual interaction matrices, one per sample (Figure 1). To precisely assess the general similarity
92 between matrices, we computed the replicability index (Yang et al., 2017) between all pairs of matrices
93 from different groups (*i.e.*, d90 vs. d110) and from the same group (see Section 4.4.1 and Supplementary
94 Methods). By considering matrices from a previous study made on liver samples in adult pigs (Foissac
95 et al., 2019), we could also compute the similarity measure between matrices from different tissues and
96 development stages. As expected, the highest replicability index was obtained between replicates from the
97 same group (0.92 on average, compared to 0.87 between groups and 0.67 between tissues). Adding counts
98 from matrices of the same group generated two high-density matrices named “merged90” and “merged110”
99 (Figure 1). More precisely, maximum matrix resolutions as defined by Rao et al. (2014) were 25 Kb on
100 average per individual sample, 15 Kb for the merged110 matrix and 10 Kb for the merged90 matrix (see
101 Methods).

102 2.2 A complex landscape of stable and group-specific TADs

103 We looked for Topologically Associating Domains (TADs) in each interaction matrix (see Section 4.4.2)
104 and identified 1,312 TADs per sample on average, with 84.7% of the genome being part of a TAD in at least
105 one of the samples. Examples are displayed in Figure 2. The median TAD size of 1,200 Kb (Supplementary
106 Table 2) was consistent with previous results in human and mouse (Dixon et al., 2012; Zufferey et al.,
107 2018). In addition, computationally-predicted CTCF binding sites accumulated at TAD extremities in the
108 expected orientation (Figure 3A, Rao et al. (2014)).

109 The number of TADs differed between samples (from 951 to 1,585 per sample and up to 1,985 in the
110 merged90 matrix, Supplementary Table 2). Part of this variability could be explained by the difference in
111 the number of interactions per matrix. Indeed, computational TAD detection is known to be sensitive to
112 variations in matrix density that can result from differences in sequencing data quantity or library complexity
113 for instance Dali and Blanchette (2017); Zufferey et al. (2018). Consistently, we observed a significant
114 correlation between the number of valid interactions and the number of TADs across samples (Pearson

115 correlation coefficient = 0.83, p -value = $9.10e^{-3}$, Figure 3B). The position of the TADs also differed
116 between samples, although the global structure appeared stable overall (Figure 2). TAD conservation across
117 cell types and model species has been widely reported and discussed with various degrees of circumspection
118 (Barutcu et al., 2015; Cubeñas Potts and Corces, 2015; Dixon et al., 2015; Doynova et al., 2017; Eres and
119 Gilad, 2020; Fraser et al., 2015; Sauerwald et al., 2020). Here, we sought to investigate TAD stability
120 within the same tissue, by comparing samples from either the same or different groups (d90 vs. d110). We
121 considered that two TADs were identical when they overlapped with each other by 90% of their length.
122 Pairwise comparisons of samples from the same group resulted in 1,785 identical TADs out of 2,625 on
123 average (68.0%). As expected, this proportion was lower when comparing samples from different groups,
124 with 1,457 identical TADs out of 2,625 on average (55.5%). Nevertheless, the observation that most of the
125 TADs are shared within any pair of samples seemed to confirm a general stability of the TAD structure.
126 This stability decreased drastically when requiring identity across more than two samples: for instance,
127 only 29.0% of the TADs (2,286 out of 7,874) were identical across all the six samples. Even accounting for
128 the presence of samples from different groups, this observed variability within the same tissue illustrates
129 the issue of estimating TAD stability using a limited number of replicates (Sauerwald et al., 2020). The set
130 of identical TADs in all six samples is provided in Supplementary File 1.

131 The difference between the proportions of identical TADs in samples from the same vs. from different
132 groups prompted us to investigate the existence of “group-specific” TADs. To find them, we considered
133 all TADs with an identical TAD in each of the three replicates within the same group but no identical
134 TAD in any replicate from the other group. This simple filtering process led us to a small set of 252
135 distinct group-specific TADs (201 for d90 and 51 for d110). It should be noted that visual inspection of
136 the interaction matrices at the corresponding genomic positions did not show striking differences in the
137 TAD patterns between groups (Figure 2). In order to confirm the consistency between the group-specific
138 TADs and the raw matrix data, we computed and compared the local Interaction Score of the group-specific
139 TAD boundaries in both groups. The Interaction Score (IS) is defined as the proportion of interactions
140 across the midpoint of a given genomic region (see Section 4.4.2) and can be used to assess the insulation
141 property of TAD boundaries (Foissac et al., 2019). We computed the IS at each TAD boundary for each
142 sample and computed the difference of the mean score between the d90 and the d110 groups (hereafter
143 referred to as “ Δ IS”). Negative Δ IS indicates a relative loss of interactions between 90 and 110 days. They
144 should therefore characterize TAD boundaries that became stronger or that appeared during gestation, as
145 one would expect for d110-specific TADs. Symmetrically, positive Δ IS indicates a gain of interactions
146 and should therefore characterize TAD boundaries that became more permissive or disappeared during
147 gestation. As expected, comparing the Δ IS values of the d90- and d110-specific TAD boundaries showed
148 that the average Δ IS was positive for boundaries of d90-specific TADs but negative for boundaries of
149 d110-specific TADs (Figure 3C). Moreover, the difference was statistically significant (p -value $< 2e^{-7}$,
150 Wilcoxon test), supporting that group-specific TADs exhibit opposite dynamics of boundary strength
151 regardless of their number.

152 Considering the drastic impact TAD boundary variations can have on development (Lupiáñez et al.,
153 2015), the TAD structure differences that we observed between 90 and 110 days of gestation are likely to
154 regulate the expression of genes involved in pig muscle maturation. Notably, we found several genes with
155 muscle-related functions in the regions that differ between overlapping group-specific TADs, including
156 *GAP43*, *PECR* and *STIM2* for instance (Guarnieri et al., 2013; Piórkowska et al., 2017; Darbellay et al.,
157 2010). The set of group-specific TADs is provided in Supplementary File 2.

158 Altogether, these results showed that, while most of the TADs were preserved when comparing samples
159 pairwise, a subset of the TADs was exclusively and consistently detected within either the d90 or the d110
160 group. The difference in the insulation capacity of their boundaries during time suggests that these TADs
161 contribute to reshaping the structural organization of the pig genome during gestation.

162 **2.3 Genome compartments identification revealed a major chromatin remodeling** 163 **during muscle maturity in pig**

164 At a higher level of organization, we investigated the segmentation of the chromosomes into A and B
165 epigenetic compartments using the interaction matrix of each replicate. We identified 682 compartments per
166 replicate on average (Supplementary Table 2) with a median size between 2.6 and 3.5 Mb, in the same order
167 of magnitude than what was reported in human or mouse cells (Dixon et al., 2012; Lieberman-Aiden et al.,
168 2009). As observed with TADs, compartment predictions were highly similar between matrices: 83.3% of
169 the genomic regions with a prediction in each of the six samples were assigned the same compartment
170 type in all of them consistently (either A or B six times, Figure 2 and Supplementary Figure 1), which is
171 significantly higher than expected by chance (p -value $< 1e^{-3}$, permutation test). These results illustrate the
172 high level of reproducibility between replicates and argue for a general conservation of the higher structural
173 organization level of the genome, as previously observed in other organisms (Barutcu et al., 2015; Dixon
174 et al., 2015; Doynova et al., 2017).

175 Despite this general consistency, a striking discrepancy appeared between groups. Indeed, for all
176 replicates, d110 compartments were systematically smaller and more abundant than d90 compartments,
177 with an increase of about 30.2% (from 593 to 772 compartments on average). A similar trend was
178 obtained by analyzing the merged matrices (from 601 to 804 compartments for merged90 and merged110
179 respectively, Supplementary Table 2). This difference in the number of compartments was observed genome-
180 wide and for both compartment types, suggesting a general fragmentation of the compartmentalization
181 during development (Figure 4A, Supplementary Figure 1 and Supplementary Table 2). Interestingly,
182 contrary to what was observed for TADs, no substantial correlation was detected between the total number
183 of interactions and that of compartments (Pearson coefficient of correlation = -0.09 , p -value = 0.84 ,
184 Figure 4B), ruling out variation in matrix density as a plausible explanation for this difference. These
185 results support the idea of a major functional switch taking place in muscle cells during the maturity
186 process, as already evidenced by expression networks (Voillet et al., 2014) and metabolomic analyses
187 (Lefort et al., 2020). Moreover, they strongly suggest that the underlying regulatory program involves
188 epigenetic modifications through a genome-wide chromatin structure remodeling.

189 To investigate the potential role of such remodeling, we used gene expression data from a previous study
190 on muscle samples at 90 and 110 days of gestation (Voillet et al., 2014). In a first step, we confirmed that
191 gene expression values were significantly higher in A vs. B compartments overall (p -value $< 2.2e^{-16}$,
192 Wilcoxon test, Figure 4C), as observed in other species (Lieberman-Aiden et al., 2009). Notably, the fact
193 that consistent results were obtained from gene expression and chromosome conformation experiments that
194 were conducted on different animals in different studies emphasizes the relevance of the data. A similar
195 difference was also obtained comparing gene density in A vs. B compartments (Supplementary Figure 2).
196 Next, we considered genomic regions with different compartment dynamics during the maturity process
197 *-i.e.*, whether they stay in the same compartment type, switch from A to B or from B to A— and compared
198 their respective dynamics of gene expression between 90 and 110 days of gestation (see Section 4.4.4).
199 Again, although expression and conformation data came from different animals, a slight yet significant
200 difference was found between groups of genes in accordance with the expected results considering the gene
201 position: genes in regions that switched from inactive (B) to active (A) compartments tend to have higher

202 fold-change expression values than those in A-to-B switching regions, with stable regions in between
203 (p -values = $1.64e^{-3}$ for the difference between A-to-B and B-to-A switches, Wilcoxon test, Figure 4D).
204 Altogether, these results suggest functional links between the genome-wide reorganization of the chromatin
205 structure and the global modification of the gene expression program that was already reported during
206 muscle maturity in pig.

207 **2.4 Comparative analysis of Hi-C maps identified significantly different interactions** 208 **between gestational stages**

209 We then performed a comparative analysis of the Hi-C matrices to identify pairs of genomic regions with
210 significantly different interaction values between groups of samples (see Section 4.4.5). This analysis led to
211 the identification of 10,183 differential interactions between pairs of 500 Kb genomic regions. While this
212 only represents 0.11% of the 9,262,199 tested interactions, the corresponding regions involved a substantial
213 proportion of the genomic space across all chromosomes (Figure 5A). Among the differential interactions,
214 8,332 (81.8%) were *cis* interactions, *i.e.*, between two genomic regions from the same chromosome. This
215 predominance is likely due to the fact that Hi-C matrices typically feature relatively low values for *trans*
216 interactions, resulting in a weaker statistical power than for *cis* interactions.

217 About 57% of the differential interactions showed a positive log-fold change (logFC), meaning that they
218 contain significantly more connections at 110 days than at 90 days. These regions are therefore expected to
219 become closer together during the 90 to 110-day transition. Inversely, negative logFC should characterize
220 pairs of regions that become more distant during development. Interestingly, despite a rather balanced ratio
221 of positive/negative logFC overall, the proportion of differential interactions with positive and negative
222 logFC was highly heterogeneous across chromosomes (Figure 5A).

223 **2.5 Regions involved in differential *cis* interactions form homogenous blocks of** 224 **chromatin compaction**

225 To further investigate the genomic distribution of significantly different interactions, we first focused
226 on *cis* differential interactions and represented them along the chromosomes depending on the sign of
227 their logFC (Figure 5B). Although each single genomic locus could potentially be involved in differential
228 interactions of opposite logFC signs (by moving from one region to another one for instance), we noted a
229 general predominance of one of the signs. More precisely, out of the 3,616 distinct 500 Kb regions involved
230 in at least one differential interaction, 2,261 of them (62.5%) have either only one type (with positive or
231 negative logFC) of interaction or at least 10 times more interactions of one type. Interestingly, regions
232 with such a predominance of one sign tended to cluster adjacently along the genome to form homogenous
233 blocks of either positive or negative differential interactions (Figure 5B). For instance, chromosomes 1,
234 13 and the q arm of chromosome 2 were largely covered by blocks of positive logFC, while blocks of
235 negative logFC could be found in large chunks of chromosomes 3, 12 and 14 (Figure 5B). We termed
236 these homogenous blocks BODIs, for Blocks Of Differential Interactions, and assigned to each of them its
237 predominant logFC sign.

238 We first wanted to assess the significance of this observation, considering that some of the differential
239 interactions with the same sign were expected to involve adjacent regions just by chance, necessarily
240 forming blocks of variable sizes. To do so, we compared the size distribution of the observed BODIs with
241 that of artificial BODIs obtained after randomly shuffling the logFC signs of the existing interactions (see
242 Section 4.4.6). We found a significant overrepresentation of both positive and negative BODIs of size
243 equal or greater than 2.5 Mb up to 5 Mb (p -value < $10e^{-3}$, permutation test, Supplementary Figure 3),
244 supporting the relevance of the observed BODIs.

245 Assuming that a drastic accumulation or depletion of pairwise interactions could result from variations
246 of chromatin density, we hypothesized that positive BODIs could indicate genomic regions that undergo
247 chromatin compaction during development. Inversely, negative BODIs would then reflect wide de-
248 condensation events along the chromosomes. We therefore checked for consistency with the positions
249 of A/B compartments. Interestingly, while BODIs could be found in every chromosome with a variable
250 proportion of positive/negative BODIs, their genomic distribution in A and B compartments seemed to
251 depend on their sign. Indeed, 58% of the genomic space in negative BODIs belonged to A compartments,
252 while this overlap was only 30% for positive BODIs. Considering that A and B compartments occupy
253 about the same size of the genome, this discrepancy between A and B compositions of BODIs was
254 highly significant (p -value $< 2.2e^{-16}$, Fisher's Exact test). Consistently, a significant difference could be
255 observed between gene expression ratios too: genes in negative BODIs had significantly higher logFC
256 values on average than genes in positive BODIs (p -value $< 2.4e^{-4}$, Wilcoxon test). These results support
257 an epigenetic control of the chromatin compaction during late development in muscle cells.

258 **2.6 Preferential clustering of telomeres at 90 days of gestation**

259 We then focused on the genomic distribution of *trans* interactions genome-wide and observed an
260 accumulation of differential interactions at the chromosome extremities, in particular with negative
261 logFC (Figure 5C and Supplementary Figure 4). These interactions involved telomeric and sub-telomeric
262 regions from both “q” and “p” arms of several chromosomes, providing additional support for a major
263 reorganization of the chromosome conformation during gestation.

264 In order to validate this model, three combinations of “p” or “q” telomeric associations between different
265 chromosomes (SSC2pter – SSC9qter, SSC13qter – SSC9qter and SSC15qter – SSC9qter) were selected
266 based on the density of differential interactions in *trans* (Figures 5C and S4) and further tested by 3D
267 DNA FISH. The number and proportion of nuclei with telomere associations were determined for each
268 combination at 90 and 110 days. Results are presented in Figure 6 and Table 1. All three tested combinations
269 revealed telomere clustering at both stages. Furthermore, for each combination, we obtained significantly
270 higher proportions of association at 90 days vs. 110 days (p -value = 0.02, χ^2 test), confirming a consistent
271 variation of the distance between these telomeres during late gestation (Figure 6 and Table 1).

3 DISCUSSION

272 **3.1 First insights in porcine muscle genome architecture during late gestation**

273 To the best of our knowledge, the present study is the first 3D genome structure assessment performed
274 on fetal muscle tissue in pig. The specific focus on the period of 14 and 4 days before birth, a critical
275 gestation time for piglet survival at birth, makes our experimental design of high relevance for agronomic
276 research (Foxcroft et al., 2006; Rehfeldt and Kuhn, 2006; Rehfeldt et al., 2000). In addition, the anatomical,
277 physiological and genetic homologies between human and pig also make it of interest for the biomedical
278 field (Lunney, 2007; Meurens et al., 2012). Related 3D genomics studies on muscle development were
279 mostly performed on mouse, using *in vitro* cell cultures (Doynova et al., 2017; He et al., 2018; Zhang et al.,
280 2020), targeting early stages (myoblasts proliferation and differentiation). Here, we focused on the maturity
281 process of differentiated muscle fibers before birth. The closest study we know in human was performed
282 on skeletal muscle (among other tissues) of adult subjects, not during development (Schmitt et al., 2016).

283 As in many studies using Hi-C assays, an obvious limitation of our experimental design is the relatively
284 low number of biological replicates, compared for instance with differential gene expression studies.
285 Considering the ongoing cost reduction of preparing and sequencing Hi-C libraries, we expect the average
286 number of replicates in Hi-C studies to increase in the future, as it has been the case for RNA-seq (Liu et al.,

287 2014; Rapaport et al., 2013). Another limitation is the presence of a female fetus among the six fetuses of
288 the study. While this heterogeneity increased the variability in one of the groups and consequently impacted
289 the statistical power of the comparative analysis, we still could observe many significant differences
290 between the two stages (see the differential interaction analysis). In addition, for A/B compartments and
291 TADs comparisons, we chose highly stringent criteria (consistently opposed predictions between groups
292 across all samples) to ensure a low false positive rate. The consistency with gene expression data from
293 another study (see A/B compartment switches) and DNA FISH experiments (see telomere clustering)
294 argue for the reliability of the results and for the structural plasticity of the porcine genome during late
295 development.

296 **3.2 TAD stability vs. variability: an open question**

297 Numerous studies have led to the widespread perception that TADs are highly conserved across cell types
298 and species (Bonev and Cavalli, 2016; Dixon et al., 2012; Rao et al., 2014; Schmitt et al., 2016). However,
299 recent reports have highlighted the variability of the TAD organization between or within species (Eres and
300 Gilad, 2020), including between biological replicates of the same tissue or cell line (Sauerwald et al., 2020).
301 Several reasons can explain this heterogeneity. First, TAD variability highly depends on the nature of the
302 samples that are being compared. As in gene expression assessment for instance, one could reasonably
303 expect samples from functionally similar tissues to generate closer results compared with samples from
304 unrelated tissues. The lack of available data is another obstacle to correctly assess TAD variability, even
305 among samples from the same tissue or cell line. Indeed, due to their high experimental cost compared with
306 other assays like RNA-seq for instance, Hi-C experiments are usually not performed on a large number of
307 replicates. Consequently, apart from some widely used human or mouse cell lines, most of the currently
308 available datasets only propose biological duplicates, in particular for tissue samples. Obviously, the lack
309 of a proper and commonly accepted definition of TADs also hampers the estimation of their variability.
310 Consistently, benchmarking studies of TAD detection methods frequently report heterogeneous results
311 (Dali and Blanchette, 2017; Zufferey et al., 2018).

312 Here, we showed that, by analyzing six samples from two different development stages of the same tissue,
313 we could survey a wide spectrum of the topological landscape. On the one hand, pairwise comparisons
314 between replicates of the same tissue –even from different gestational stages– resulted in a majority of
315 identical TADs, thereby supporting the idea of a stable topological landscape. Moreover, we could identify
316 a subset of highly stable TADs that were consistently detected in all samples regardless of the group. On
317 the other hand, only a small proportion of the TADs (less than one third) fell into this category, meaning
318 that the vast majority could not be found in all the samples. Also, we could identify a subset of variable
319 TADs that were consistently group-specific, potentially enabling regulatory programs of gene expression.
320 The presence of several genes with muscle-related function in the variable regions of these group-specific
321 TADs supports this hypothesis, and provides interesting candidates for further functional investigations.
322 Besides transcriptional regulation, part of this TAD variability could also be due to mechanisms like DNA
323 replication and repair (McCord et al., 2020), which are particularly active during fetus development.

324 Overall, due to the limited relevance of any general statement on TAD variability/stability, the main
325 challenge is probably less about estimating how variable/stable TADs are than about identifying which
326 TADs can reliably be considered as variable/stable. In this context, ongoing efforts in data production
327 and analysis are providing substantial help to complete and explore the known panorama of chromatin
328 topologies, including in farm species (Giuffra et al., 2019). As for any functionally relevant genomic
329 feature, the capacity to distinguish stable from variable TADs is undoubtedly an important asset to decipher
330 the molecular mechanisms underlying their formation, regulation and conservation.

331 **3.3 Switching compartments in muscle nuclei during late gestation**

332 We confirmed several known features of A/B genome compartments related to gene density, expression,
333 and general stability across replicates (Barutcu et al., 2015; Doynova et al., 2017; Foissac et al., 2019;
334 Lieberman-Aiden et al., 2009). Although the median size of our compartments was in line with previous
335 reports (Dixon et al., 2012; Foissac et al., 2019; Lieberman-Aiden et al., 2009), a decrease of the
336 compartment size was observed at the end of gestation in our fetal samples, suggesting a fragmentation of
337 the compartments. We observed about 3% of the genomic regions that underwent a total and consistent
338 compartment switch considering the three replicates of each condition. These dynamic changes seem
339 less important compared with some studies where extensive A/B compartment switches were observed.
340 For instance, up to 25% of switches were reported in pairwise comparisons between human embryonic
341 stem (ES) cells and mesenchymal stem cells (MSCs) (Dixon et al., 2015), 12% between epithelial and
342 breast cancer cells (Barutcu et al., 2015), and from 8% to 21% between progenitor and differentiated
343 myotubes (Doynova et al., 2017; He et al., 2018). However, in these studies, the switching regions were
344 identified after merging all replicates for each condition without considering consistency across replicates.
345 Moreover, the A/B compartments were identified at different resolutions in each study (from 40 Kb to
346 500 Kb). Fine changes that cannot be observed at low resolutions might be detected by using smaller bin
347 sizes, consequently increasing the number of variable genome regions. On the other hand, high resolution
348 analyses require a large amount of data. False positive switches are expected in genomic regions with low
349 read coverage for instance, especially in pairwise comparisons of merged samples that do not take biological
350 replicates into account. This could partly explain the higher percentages of switching compartments found
351 in previous studies. Nevertheless, cell or tissue type is likely the main driver of compartment variability, as
352 shown for TAD structures (Sauerwald et al., 2020). In Dixon et al. (2015) for instance, mesendoderm (ME)
353 cells and MSCs showed 3.8% and 25% of switches respectively compared with their ES progenitors cells,
354 suggesting that the more divergent the cell populations, the more important the differences in chromatin
355 structure. In this context, while our study features a relatively low proportion of compartment switches,
356 the consistency across replicates plus the fact that all cell populations come from the same tissue type
357 (differentiated muscle fibers from late development stages) strongly argue for a biological significance
358 of these results. The consistency with previously obtained gene expression results (associating opposite
359 expression dynamics to genes in symmetrical compartment switches) further supports the role of chromatin
360 structure on gene expression, in agreement with previously reported results in human and mouse (Barutcu
361 et al., 2015; Dixon et al., 2015; Doynova et al., 2017; He et al., 2018; Won et al., 2016).

362 **3.4 Dynamic interacting genomic regions during the maturity process of fetal muscle**

363 In this study, we could detect genome-wide dynamic changes in the chromatin structure of muscle nuclei
364 occurring at late gestation. Specifically, we identified 10,183 differential interactions at 500 Kb resolution
365 between the 90th and the 110th day of gestation. As noted above, considering our model of differentiated
366 muscle fibers at two relatively close developmental stages, minor differences could have been expected. For
367 instance, we detected much more differentially interacting regions compared with the murine myogenesis
368 *in vitro* model (Doynova et al., 2017; He et al., 2018), where only 55 and 2,609 differential interactions
369 were reported between myoblasts and differentiated myotubes respectively.

370 The differential interactions were distributed all over the genome but not homogeneously. We observed
371 large genomic regions of adjacent differential interactions with the same dynamic behavior when comparing
372 the two gestational ages, sometimes along entire chromosome arms. Similar results were observed on
373 the fly genome, where higher-order clusters corresponding to each chromosome arm were organized into
374 active and inactive clusters (Sexton et al., 2012). However, those results were not associated to dynamic
375 changes as the fly study was focused on an exhaustive description of 3D folding features rather than on a

376 comparison between two different conditions. This chromatin remodeling of large adjacent regions might
377 be involved in the transcriptional and metabolic changes previously observed in fetal pig muscle (Lefort
378 et al., 2020; Voillet et al., 2014, 2018).

379 Interestingly, we found that 58% of the genomic space in the negative BODIs was located in A
380 compartments compared with only 30% for positive BODIs. To explain these results, we hypothesize that
381 the structural and functional environment of A and B compartments may induce changes on the chromatin
382 state of local regions located inside each compartment type. For instance, following our definition that
383 negative BODIs are genomic regions that were closer (more condensed) at 90 days of gestation and
384 that become farther apart at the end of gestation, we propose that those negative BODIs located on a
385 decondensed/active environment (A compartment) follow a chromatin activation/de-condensation through
386 development promoted by the genomic active environment.

387 **3.5 Inter-chromosomal telomeres clustering**

388 We found multiple dynamic associations between the telomeric regions (telomeres clustering) of several
389 chromosomes involving either the p or the q arm. The density of interactions between telomeres decreases
390 at 110 days of gestation. Nevertheless, 3D DNA FISH analyses do not suggest a dissociation of the clusters
391 at the end of gestation but a higher prevalence of telomeres clustering at 90 days of gestation compared
392 with 110 days. This indicates that telomeric regions exhibit a dynamic coordinated nuclear organization in
393 muscle cells during late development. In fact, telomeres have been observed to display rapid movements in
394 live human cells (Wang et al., 2008).

395 Interactions between telomeric regions have been widely reported in several species: preferential contacts
396 between telomeres have been reported in fly embryonic nuclei, although these contacts were not associated
397 with dynamic changes (Sexton et al., 2012). Another study showed that telomeric and sub-telomeric regions
398 exhibit more frequent interactions in epithelial cells than in breast cancer cells (Barutcu et al., 2015). In
399 this latter study, however, only intra- but not inter-chromosomal interactions were reported, meaning that
400 some chromosomes bend to bring their extremities in contact with each other. This chromosome bending
401 phenomenon was also reported in pig neutrophils (Mompert et al., 2013). Besides, the telomeres clustering
402 has also been observed in yeast meiotic and quiescent cells (Guidi et al., 2015; Lazar-Stefanita et al., 2017;
403 Yamamoto, 2014). In yeast, the telomere clustering has been associated to the formation of foci in which
404 silencing factors concentrate, and the dynamic nature of aggregation or dissociation of these clusters has
405 been also demonstrated (Hozé et al., 2013). Further evidences of telomere clustering have been found in
406 mammals both in somatic cells and gametes (Solov'eva et al., 2004). For instance, in human cancer and
407 mouse cell lines, dynamic associations and dissociations of telomere fractions were observed in quiescent
408 cells (Molenaar et al., 2003); in human fibroblasts, telomeres were found preferentially associated in
409 interphase nuclei than in their cycling counterparts (Nagele et al., 2001); and in pig, a strong clustering of
410 telomeres was reported in differentiated immune cells like neutrophils and lymphocytes (Yerle-Bouissou
411 et al., 2009).

412 Interestingly, in human myoblasts, long telomeres have been observed to be involved in forming
413 chromosome loops that can affect the higher order chromatin structure and gene expression (Robin et al.,
414 2014). It was proposed that telomere length-dependent long-range chromosomal interactions may repress
415 (or enhance) gene expression by respectively silencing (or activating) those genes close to the telomere
416 when telomeres become shorter with cellular aging. Besides, the SMARCA4 subunit of the SWI/SNF
417 complex, which has a potential role in tissue-specific gene regulation during embryonic development,
418 has been suggested to play a role in three-dimensional organization of telomeric regions (Barutcu et al.,
419 2016). In addition, the ATPase subunit of this same SWI/SNF complex has been found to be required

420 for the formation of inter-chromosomal interactions contributing to changes in gene positioning during
421 myogenesis and temporal regulation during myogenic transcription (Harada et al., 2015). Our finding of
422 inter-chromosomal clustering of telomeric regions during late gestation, together with the aforementioned
423 studies related to telomere associations, raise the possibility of a specific dynamic mechanism of gene
424 expression regulation in fetal muscle cells through temporal formation-disruption of telomere clusters.

425 In conclusion, we found major changes of the 3D genome structure during the establishment of muscle
426 maturity at late gestation. These changes occur concomitantly with previously reported modifications
427 of the transcriptional program, between 90 and 110 days of gestation. The topological reorganization
428 that we observed implies structures of various scales, including individual interactions, TADs and large
429 BODIs. The proportion of the genome that was impacted depended on the nature of the modification.
430 Some of the changes, such as the fragmentation of the genomic A/B compartments, impacted most of
431 the chromosomes, while others, such as the telomere clustering, involved specific regions. The amplitude
432 of these modifications is particularly striking considering that two close fetal development stages were
433 compared. This suggests that topological changes of the 3D genome of organized tissues could be as
434 remarkable as changes observed during cell differentiation and cell commitment.

4 MATERIALS AND METHODS

435 Experimental and computational resources used in this study are listed in Supplementary Table 3, including
436 names of chemical reagents, kits and software versions.

4.1 Animals and samples

438 For Hi-C and FISH experiments, *longissimus dorsi* fetal porcine muscle samples were collected from
439 the European Large White (LW) breed (F1 ♂LW x LW♀). Specifically, three 90 days gestation male
440 littermates and three 110 days gestation (two male littermates and one female) were used for Hi-C assays.
441 For FISH experiments, muscle samples were collected from different fetuses (one at 90 days gestation and
442 one at 110 days) of those in which Hi-C experiments were performed. All the fetuses used in this study
443 were obtained by caesarean after euthanasia of healthy wild type sows and fetuses. No special breeding
444 conditions (feeding, housing, treatment) were applied.

445 The experimental design was approved and authorized by the ethical committee (#84) in animal
446 experimentation of the French Ministry of National Education, Higher Education, and Scientific Research
447 (authorization #02015021016014354). The experiment authorization number for the experimental farm
448 GenESI (Genetics, testing and innovative systems experimental unit) is A17661. The procedures
449 performed in this study and the treatment of animals complied with European Union legislation (Directive
450 2010/63/EU) and French legislation in the Midi-Pyrénées Region of France (Decree 2001-464). All
451 the details about the animals and samples have been registered in the BioSamples public repository
452 (<https://www.ebi.ac.uk/biosamples>) in agreement with the FAANG best practices guidelines
453 (<https://www.faang.org/data-share-principle>) and are available using the accession
454 SAMEA7390788.

4.2 3D DNA FISH experiments

4.2.1 Cells and probes preparation

457 Fetal muscle tissue was obtained from the *Longuissimus dorsi* muscle of 90- and 110-days of gestation
458 Large White (LW) pig and prepared as described in Lahbib-Mansais et al. (2016); Marti-Marimon et al.
459 (2018). Stored muscle fibre packets were permeabilised for 5 to 8 min in cytoskeleton extraction buffer (100
460 mM NaCl, 300 mM sucrose, 3 mM MgCl₂, 10 mM PIPES pH 6.8) containing 0.5% Triton X 100 and then
461 fixed in cold 4% paraformaldehyde for 5 min. After washing in cold PBS, muscle packets were manually

462 dilacerated directly on Superfrost glass slides (CML, Nemours, France) to isolate individual fibres, and
463 air-dried before adding DNA probes for in situ hybridization. Bacterial artificial clones (BACs) containing
464 specific subtelomeric sequences of porcine chromosomes 2, 9, 13 and 15 were chosen as selected by
465 Mompert et al. (2013): SSC2p (PigI-370D12), SSC9q (PigI-441D12, PigI-564B6), SSC13q (PigI-39F7)
466 and SSC15q (PigI-899B10). These BACs were isolated from a porcine BAC library (CRB-Anim, INRA,
467 2018. Biological Resource Centres for domestic animals of AgroBRC, doi: [http://doi.org/10.](http://doi.org/10.15454/1.5613785622827378E12)
468 [15454/1.5613785622827378E12](http://doi.org/10.15454/1.5613785622827378E12)). For multiple-label experiments, approximately 120 ng of each
469 BAC DNA was random-priming labelled directly by incorporation of dUTP Alexa Fluor (488 or 568)
470 or indirectly with Biotin-6-dUTP detected by immuno-FISH (Bioprime DNA labelling kit, Invitrogen,
471 Cergy Pontoise, France). Three combinations of p or q telomeres probes of different pairs of chromosomes:
472 (SSC2qter – SSC9qter), (SSC13qter – SSC9qter) and (SSC15qter – SSC9qter) were chosen to test their
473 rate of association as suggested by Hi-C.

474 4.2.2 3D DNA Fluorescence In Situ Hybridization

475 3D DNA FISH experiments were conducted as described in Lahbib-Mansais et al. (2016) with slight
476 modifications. Probes were resuspended in hybridization buffer (50% formamide, 10% dextran sulphate,
477 2 mg/ml BSA, 2× SSC) at a final concentration of 110 ng/μl. Nuclear DNA of fibers and probes were
478 simultaneously heat-denatured at 74 °C for 7 min on the slide and then incubated overnight at 37 °C in a
479 DAKO hybridizer. Post-hybridization washes were then performed with gentle agitation, first twice in 2×
480 SSC at 40°C for 6 min, then in 2× SSC, 50% formamide pH 7.0 at 40°C for 6 min, and finally twice for 10
481 min in 2× SSC, then in PBS at RT. When a biotin labelled probe was used, biotins were detected with
482 streptavidin Alexa 568 or 488 at a final concentration of 5 μg/ml for 1 hour at RT.

483 3D acquisitions were performed at the T.R.I. Genotoul (Toulouse Réseau Imagerie, [http://](http://trigenotoul.com/en)
484 trigenotoul.com/en) imaging core facility in Toulouse (France). Image stacks were collected
485 using a Leica SP8 confocal microscope (Leica Instruments, Heidelberg, Germany) equipped with an oil
486 immersion objective (plan achromatic 63× N.A. = 1.4). The Z-stacks (around 80 confocal planes per
487 capture) were acquired at 1024 × 1024 pixels per frame using an 8-bit pixel depth for each channel at a
488 constant voxel size of 0.06 × 0.06 × 0.3 μm.

489 4.2.3 Telomere association analysis

490 Images were analyzed with specific software NEMO (Iannuccelli et al., 2010), distributed under the
491 creative commons license that can be freely downloaded from [https://forge-dga.jouy.inra.](https://forge-dga.jouy.inra.fr/projects/nemo)
492 [fr/projects/nemo](https://forge-dga.jouy.inra.fr/projects/nemo). Segmentations and 3D measurements between signals (center-to-center distance)
493 were done as described in Lahbib-Mansais et al. (2016). Euclidean distances were computed with respect to
494 the x , y and z resolutions. Given the resolution on the z axis, at least three pixels corresponding to 0.9 μm
495 (0.3 × 3) were required for a high resolution between two separate signals; consequently, 1 μm was chosen
496 as the upper cut-off for associated signals. For each combination of telomeres, nuclei were only analyzed
497 when 4 signals (corresponding to the chosen telomeres of 2 chromosomes) were present. “Associated”
498 signals were considered when they are separated by a distance (d) ≤ 1 μm, as done in Lahbib-Mansais et al.
499 (2016). We determined for each combination of telomeric pairs how many nuclei were found associated
500 among about 100 observed nuclei.

501 Significance of the difference in association between d90 and d110 was assessed using a χ^2 test to
502 compare generalized linear models of the binomial family with a fixed telomeric pair covariate and
503 including, or not, the condition as a second covariate (see Supplementary Methods).

504 4.3 Hi-C experiments

505 4.3.1 Hi-C protocol

506 Hi-C experiments were performed as previously documented (Foissac et al., 2019), with slight
507 modifications to adapt the Hi-C experiments and libraries to fetal muscle tissues (see Supplementary
508 Methods).

509 4.3.2 Hi-C Quality controls

510 After DNA digestion with HindIII, and filling-ligation of the digested ends, the HindIII target
511 site disappears and a NheI restriction site is created instead. To check the efficiency of the Hi-C
512 assays, PCR were performed around one HindIII restriction site with two forward primers (Fwd1: 5'
513 TCTGGGCAGGTCACCTATT 3'; Fwd2: 5' TCTCGGGATGCTGAGTGTTT 3'; product size = 425 bp).
514 A reverse primer combined with Fwd1 was used as a control (Rv1: 5' AAACACTCAGCATCCCGAGA 3';
515 product size = 465 bp). In Hi-C, some religation events allow switching the sense of one DNA fragment
516 and PCR amplification with the two forward primers. The PCR amplification products from the couple
517 of forward primers were digested either with HindIII or NheI (product sizes = 201 + 215 bp). In control
518 tubes (no filling of digested ends), HindIII should cleave the PCR products while NheI should not. In Hi-C
519 tubes, NheI should cleave most of the PCR products while HindIII should cleave only a small fraction.

520 4.3.3 Hi-C library production

521 1.4 μ g of DNA from the Hi-C experiments were fragmented with a Covaris machine. Then, 0.55 volumes
522 of CleanPCR magnetic beads were added to the fragmented DNA to select fragments < 600 bp (5 min
523 incubation and keeping the supernatant), and 0.7 volumes of beads were added again (5 min incubation
524 and removing supernatant) to remove fragments < 200 bp. Then beads were washed with 80% ethanol
525 and DNA was recovered with Resuspension Buffer. To purify biotinylated DNA, 1 volume of M-280
526 streptavidin magnetic Dynabeads was added and after 15 min incubation, the supernatant was removed and
527 the beads were washed 4 times with beads wash buffer (Nextera Mate Pair Preparation Kit, Illumina) and
528 twice with Resuspension buffer. From this point, all steps were performed while DNA remained attached to
529 the beads. To repair DNA breaks, 60 μ l of water and 40 μ l of End Repair Mix 2 (TruSeqNano DNA library
530 prep, Illumina) were added and incubated 30 min at 30 °C, and then beads were washed as explained
531 before. To allow the adapters ligation, an "A" nucleotide was added to the 3' ends by adding 17.5 μ l of
532 water and 12.5 μ l of A-Tailing Mix (TruSeqNano DNA library prep, Illumina) and incubating 30 min at 37
533 °C and then 5 min at 70 °C to inactivate the enzyme. To ligate the adapters to the DNA extremities, 2.5 μ l
534 of Resuspension Buffer, 2.5 μ l of DNA Ligase Mix and 2.5 μ l of DNA Adapter Index (TruSeqNano DNA
535 library prep, Illumina) were added (10 min incubation at 30 °C, then 5 μ l of Stop ligation Buffer) and then
536 beads were washed as before. DNA was amplified by 12 PCR cycles (15 sec at 98 °C – 30 sec at 60 °C –
537 30 sec at 72 °C) by resuspending beads in 50 μ l of PCR mix (25 μ l Enhanced PCR mix, 5 μ l PCR primer
538 Cocktail and 20 μ l water, TruSeqNano DNA library prep, Illumina). To recover DNA from the beads, 0.6
539 volumes of CleanPCR magnetic beads were added and incubated 5 min, and then washed twice with 80%
540 ethanol, resuspended in 30 μ l of Resuspension Buffer and after placing in a magnetic rack, supernatant
541 containing the libraries was recovered. Libraries size was controlled with the Fragment Analyzer (FA) and
542 quantified by qPCR. In addition, an aliquot was digested by using the NheI and HindIII enzymes to verify
543 if selected fragments are the ones containing the filled-in biotinylated religation sites as done in Belton
544 et al. (2012). Libraries were sequenced in pool in one HiSeq3000 lane to validate their quality. For depth
545 sequencing, the pool was paired end (PE) sequenced in 11 lines of a HiSeq3000 (reads size = 150 bases),
546 producing from ~ 476 M to 685 M read pairs per library in total (see Supplementary Table 2).

547 **4.4 Hi-C data analysis**548 **4.4.1 Hi-C reads and interaction matrices**

549 The 3,447,428,742 Paired-End reads were processed using HiC-Pro v2.9.0 (Servant et al., 2015) as
550 previously reported (Foissac et al., 2019). The bioinformatics analysis includes the following steps (see
551 Supplementary Methods for more details).

- 552 • Read mapping was performed on the Sscrofa11.1 genome assembly version using Bowtie 2 v2.3.3.1
553 (Langmead and Salzberg, 2012).
- 554 • Interaction matrices were generated from valid pairs at various resolutions depending on the bin
555 size. Most of the subsequent analyses were performed at the 500 Kb resolution apart from few
556 exceptions (TAD detection for instance was performed at the 50 Kb resolution). A total of 6 interaction
557 matrices were obtained per resolution ($n = 3$ (replicates) $\times 2$ (groups)). Additionally, merged
558 interaction matrices were computed by summing the interaction values of the 3 matrices for each
559 group. Considering the high number of unassembled scaffolds in the pig genome Sscrofa11.1 version
560 and given the fact that samples from both genders were collected, we focused our analysis on the 18
561 assembled autosomes to avoid potential effects of the sexual chromosomes on the results.
- 562 • Interaction matrices were displayed using Juicebox (Durand et al., 2016) and **HiTC R** / Bioconductor
563 package v1.18.1 (Servant et al., 2012).
- 564 • Interaction matrices were normalized per chromosome using the non-parametric iterative correction
565 and eigenvector decomposition (ICE) method when needed (Imakaev et al., 2012).
- 566 • Replicability between interaction matrices was assessed using the replicability index of Yang et al.
567 (2017) as implemented in the R / Bioconductor package **hicrep**.
- 568 • Maximal resolution was computed following Rao et al. (2014): a given resolution (bin size) can be
569 claimed if, at that resolution, 80% of the bins or more contain at least 1,000 interactions. The proportion
570 of bins with a cumulated number of valid interactions higher than 1,000 was therefore computed
571 for different resolutions (from 100 to 5 Kb) for each individual (sample) and for the merged (group)
572 matrix.

573 **4.4.2 TADs calling and comparison**

574 TADs were predicted per chromosome from raw interaction matrices ($n = 3$ (replicates) $\times 2$ (groups)
575 $\times 18$ (autosomes)) at 50 Kb resolution with the Arrowhead method of the Juicer tool v1.5.3, using the
576 $-k$ KR parameter to ensure matrix balancing normalization. TAD finding was performed on individual
577 matrices of each replicate separately (to assess group replicability) and on the merged matrices ($n = 2$
578 (groups) $\times 18$ (autosomes)) to obtain a set of TADs for each group (90/110 days of gestation). To identify
579 TADs that are consistently predicted from different replicates and group-specific TADs, we performed
580 pairwise comparisons of TAD sets from different replicates using bedtools (v2.26.0). A mutual overlap of
581 90% similarity was required with the parameters $-f 0.9 -r$.

582 Insulation capacity of TAD boundaries was computed as previously described (Foissac et al., 2019) using
583 the local interaction score. In brief, considering all valid interactions around the same TAD boundary (*i.e.*,
584 both reads being not further than 500 Kb from the boundary) the interaction score corresponds to the
585 proportion of valid interactions across the boundary. IS scores were normalized by cyclic loess (Ballman
586 et al., 2004) using **csaw** (Lun and Smyth, 2015) (see Supplementary Methods for more details).

587 4.4.3 CTCF prediction

588 The position specific frequency matrix corresponding to the CTCF-binding motif was recovered from
589 the JASPAR Transcription Factor Binding Sites (TFBS) catalogue (<http://jaspar.genereg.net>,
590 Mathelier et al. (2016)). CTCF genomic occurrences were predicted by running FIMO v.4.11.1 Grant et al.
591 (2011) with the JASPAR CTCF frequency matrix on the Sscrofa11.1 genome. Then, the average density
592 of CTCF predicted motifs with respect to TAD positions was obtained using bedtools v2.26.0 map and
593 coverage functions Quinlan (2014).

594 4.4.4 A/B compartments detection

595 A and B compartments were obtained using the PCA approach described in Lieberman-Aiden et al.
596 (2009), as implemented in the R / Bioconductor package **HiTC** (Servant et al., 2012). A/B compartment
597 identification was performed on intra-chromosome interaction matrices at 500 Kb resolution on individual
598 interaction matrices ($n = 3$ (replicates) $\times 2$ (groups) $\times 18$ (autosomes)) and on the merged interaction
599 matrix ($n = 18$ autosomes). Boundaries between A and B compartments were identified according to the
600 sign of the first PC (eigenvector). Bins that were not assigned to any compartment due to a lack of data
601 in some samples were not considered in subsequent integrative analyses. As an additional control, A/B
602 compartments were also obtained by using the eigenvalue method of the Juicer tool (Durand et al., 2016),
603 which lead to similar results.

604 The difference between the number of compartments in the two groups was assessed with a Poisson
605 GLM: $\log(y_{ijk}) \sim \alpha c_{ijk} + \beta_k$, with y_{ijk} the number of compartments in chromosome j from sample i
606 in group k , c_{ijk} the total number of valid interactions in chromosome j from sample i in group k , α its
607 estimated effect on the number of compartments, and β_k the estimated effect of the group on the number
608 of compartments, which was tested for being significantly different from 0 (test with $n = 2$ (groups) $\times 3$
609 (samples) $\times 18$ (chromosomes) observations).

610 4.4.5 Detection of differential interactions

611 A differential analysis was performed to extract interactions that were significantly differentially
612 connected between the two groups (90 and 110 days of gestation). This analysis was performed on
613 raw count data from the 18 autosomes at the 500 Kb resolution (the differential analysis was thus performed
614 with 2 groups and $n = 3$ replicates in each group). A method similar to the one described in Lun and
615 Smyth (2015), with some adaptations, was used to perform this task. In brief (see Supplementary Methods
616 for more details):

- 617 • Low count interactions with less 30 reads across the 6 samples (5 reads per sample on average) were
618 discarded from the analysis.
- 619 • Interaction values were normalized using a non-linear normalization method Ballman et al. (2004)
620 based on a fast cyclic loess algorithm implemented in the R / Bioconductor package **csaw** (Lun and
621 Smyth, 2016).
- 622 • Differential analysis was performed using a Generalized Linear Model (GLM) based on the Negative
623 Binomial (NB) distribution with a group fixed effect (two-level factor: 90/110 days). The model was
624 estimated with the implementation of the R / Bioconductor package **edgeR** (McCarthy et al., 2012;
625 Robinson et al., 2010) and log ratio tests were used to assess the significativity of the group effect on
626 each bin pair interaction. p -values were genome wide corrected using (Benjamini and Hochberg, 1995)
627 procedure to control the False Discovery Rate (FDR).

628 4.4.6 Characterization of BODIs

629 As a single genomic bin can be involved in multiple Differential Interactions (DI) genome-wide with
630 various logFC values, we looked for bins with a large prevalence of interactions of the same logFC sign,
631 either mostly positive or mostly negative. A minimum ratio of 90% of DI with the same sign was required
632 to identify “positive” or “negative” bins, possibly indicating regions that undergo a chromatin contraction
633 or opening, respectively. Bins with a mixture of positive and negative DI were considered as undefined.
634 Adjacent bins with the same sign (either positive, negative, or undefined) were merged into Blocks Of
635 Differential Interactions (BODIs). This analysis was performed considering only intra-chromosomal DIs
636 (in *cis*).

637 To assess the existence of an enrichment of large positive and negative BODIs given the relative
638 proportions of positive and negative individual DIs, a permutation test was performed: at each permutation,
639 logFC values were shuffled genome-wide across DIs. The same 10:1 threshold was applied to define
640 prevalently positive and negative bins and adjacent bins of the same type were merged to identify “expected
641 BODIs” under the null hypothesis (no specific trend of positive/negative bins to cluster consecutively). The
642 resulting size distributions of positive, negative and undefined BODIs were compared with that of observed
643 BODIs, and the *p*-value was computed, as the number of times expected BODIs were at least as frequent as
644 the observed ones across 100 permutations for a given size and type.

645 The comparison of BODIs with A/B compartments was done by computing the proportion of the positive,
646 negative and undefined BODIs that overlapped A or B compartments in terms of genomic space. The
647 resulting block composition was therefore obtained using the bedtools coverage function on BODIs of each
648 size and compartments of each type. As most of the compartmentalization is stable across samples, the
649 A/B compartments obtained on the merged general matrix was used. Since A and B compartments cover
650 roughly the same genomic space in total, no large difference should be observed between the A and B
651 composition of positive and negative BODIs. Significance was assessed using Fisher’s exact test between
652 the compartment type (A/B) and the BODI types (positive/negative).

653 4.5 Gene expression integrative analysis

654 4.5.1 Expression data

655 Expression data were obtained from a previous transcriptome study of skeletal muscle in pig during
656 development using microarrays (Voillet et al., 2014). The dataset consists of 44,368 probe measurements
657 for 17 samples (LW animals) at two different gestational stages: 8 samples at 90 days and 9 samples at 110
658 days. A precise description of the experimental design and data collection can be found in Voillet et al.
659 (2014). Normalized expression data (\log_2 transformed) and sample information are available in NCBI
660 (GEO accession number GSE56301). \log_2 transformed expressions and log fold change (logFC) of these
661 expression values at 90 vs. 110 days (reference time point: 90 days) were used in our integrative analyses.
662 Since the microarray was originally designed on a former version of the pig genome, probes were remapped
663 on the Sscrofa1.1 assembly version and further filtered (see Supplementary Methods for more details).

664 4.5.2 Density and expression level of genes in A/B compartments

665 To compare the gene density in A vs. B compartments, a gene density value was first computed for each
666 compartment by dividing the number of distinct gene IDs included in the compartment (using bedtools
667 map) by the size of the compartment. Resulting gene density distributions were then compared between
668 A and B compartments. Normality of the gene density was tested using Shapiro-Wilk normality test and
669 rejected for all types of compartments in both groups (*p*-values $< 2.2e^{-16}$ overall, for $n = 349$ and 322
670 A and B compartments respectively). Wilcoxon tests were then used to assess the significance of the
671 difference in gene density in A vs B compartments.

672 To compare the average gene expression in A vs. B compartment, we computed for each compartment the
673 mean expression value of its genes using bedtools map separately for the two gestational ages. Normality
674 of the average gene expression was tested using Shapiro-Wilk normality tests and rejected for both A and
675 B compartments (p -values = $2.58e^{-5}$ and $1.08e^{-3}$ for $n = 344$ and 292 A and B compartments with at
676 least one expressed gene, respectively). Wilcoxon tests were then used to assess the significance of the
677 difference in gene expression in A vs B compartments.

678 To investigate the dynamic of expression in compartment-switching regions, we considered the logFC
679 expression values of the genes and split them into compartment-switching categories using bedtools:
680 no switch, A to B, B to A. Normality of the logFC expression values was tested using Shapiro-Wilk
681 normality tests for genes in all types of compartments except for compartments with no switch ($n = 7, 511$
682 genes in these compartments, above the applicability condition of the test) and rejected for both types of
683 compartments (p -values = $1.2e^{-3}$ and $4.6e^{-6}$, for $n = 60$ and 174 genes in compartments switching from
684 A to B and from B to A, respectively). Wilcoxon tests were then used to assess the significance of the
685 difference in logFC expression values in each compartment type.

CONFLICT OF INTEREST STATEMENT

686 The authors declare that the research was conducted in the absence of any commercial or financial
687 relationships that could be construed as a potential conflict of interest.

AUTHOR CONTRIBUTIONS

688 M.B-M, M.M-M, Y.L-M and S.F. conceived the study. M.M-M and Y.L-M designed and supervised the
689 experiments. M.M-M performed the Hi-C experiments, Y.L-M and S.C. performed the 3D DNA FISH
690 experiments. S.F. and N.V. designed and supervised the data analysis. S.F., N.V., M.Z., M.M-M and D.R.
691 performed the bioinformatics and statistical analyses. M.M-M, S.F., N.V., M.B-M and Y.L-M wrote the
692 manuscript with the input from all authors.

FUNDING

693 Tissue sampling and Hi-C library sequencing were funded by the 2014 Animal Genetics Division AAP
694 grant (INRA, France), and by the “Osez l’interdisciplinarité !” grant of P. Neuvial’s SCALES project
695 (CNRS, France). Animals were raised in the experimental farm GenESI (INRAE, France).

ACKNOWLEDGMENTS

696 Hi-C libraries were produced and sequenced at the GeT-PlaGe facility (INRAE, France). Image acquisitions
697 for FISH experiments were performed at the T.R.I. Genotoul imaging core facility (Toulouse, France) and
698 computational environment was provided by the Genotoul bioinformatics platform (Toulouse, France).
699 Further support was provided to M.M-M with a training program founded by the “Soutien à la mobilité
700 internationale” scholarship from the INP (Toulouse, France) and hosted by M. Groenen’s group (WUR,
701 Netherlands). We would like to thank L. Liaubet’s team (INRAE, France) for providing samples and
702 assisting with the experiments, H. Acloque (INRAE, France) for pioneering the Hi-C in our institute, and
703 both the ChrocoGen working group and the FAANG community for their support.

704 <http://home.frontiersin.org/about/author-guidelines#SupplementaryMaterial>

DATA AVAILABILITY STATEMENT

705 Animals and samples metadata have been registered at BioSamples ([https://www.ebi.ac.uk/](https://www.ebi.ac.uk/biosamples)
706 biosamples) and are available using the accession ID SAMEA7390788. Experimental protocols have

707 been deposited at the FAANG DCC: https://data.faaang.org/api/fire_api/samples/
708 [INRAE_SOP_pig_muscle_tissue_sampling_20200812.pdf](https://data.faaang.org/api/fire_api/samples/INRAE_SOP_pig_muscle_tissue_sampling_20200812.pdf) (sampling) and
709 https://data.faaang.org/api/fire_api/assays/INRAE_SOP_Hi-C_pig_muscle_tissue_20200812.pdf (Hi-C libraries).
710 Raw sequencing data from Hi-C experiments have been uploaded to the ENA under the accession
711 PRJEB40576 (ERP124229) and to the FAANG DCC along with the associated metadata, as per the
712 FAANG consortium agreement (<https://www.faaang.org/data-share-principle>).

713 Hi-C matrices, TADs and A/B compartments generated in this study have been made
714 available at: <https://doi.org/10.15454/DOMEHB> and [http://www.fragencode.org/](http://www.fragencode.org/pig3Dgenome.html)
715 [pig3Dgenome.html](http://www.fragencode.org/pig3Dgenome.html).

REFERENCES

- 716 Ballman, K. V., Grill, D. E., Oberg, A. L., and Therneau, T. M. (2004). Faster cyclic loess: normalizing
717 RNA arrays via linear models. *Bioinformatics* 20, 2778–2786. doi:10.1093/bioinformatics/bth327
- 718 Barutcu, A. R., Lajoie, B. R., Fritz, A. J., McCord, R. P., Nickerson, J. A., Van Wijnen, A. J., et al. (2016).
719 SMARCA4 regulates gene expression and higher-order chromatin structure in proliferating mammary
720 epithelial cells. *Genome Research* 26, 1188–1201. doi:10.1101/gr.201624.115
- 721 Barutcu, A. R., Lajoie, B. R., McCord, R. P., Tye, C. E., Hong, D., Messier, T. L., et al. (2015). Chromatin
722 interaction analysis reveals changes in small chromosome and telomere clustering between epithelial
723 and breast cancer cells. *Genome Biology* 16, 214. doi:10.1186/s13059-015-0768-0
- 724 Belton, J.-M., McCord, R. P., Gibcus, J. H., Naumova, N., Zhan, Y., and Dekker, J. (2012). Hi-C: a
725 comprehensive technique to capture the conformation of genomes. *Methods* 58, 268–276. doi:10.1016/j.
726 ymeth.2012.05.001
- 727 Benjamini, Y. and Hochberg, Y. (1995). Controlling the false discovery rate: a practical and powerful
728 approach to multiple testing. *Journal of the Royal Statistical Society Series B* 57, 289–300
- 729 Bolzer, A., Kreth, G., Solovei, I., Koehler, D., Saracoglu, K., Fauth, C., et al. (2005). Three-dimensional
730 maps of all chromosomes in human male fibroblast nuclei and prometaphase rosettes. *PLoS Biology* 3,
731 e157. doi:10.1371/journal.pbio.0030157
- 732 Bonev, B. and Cavalli, G. (2016). Organization and function of the 3D genome. *Nature Reviews Genetics*
733 17, 661–678. doi:10.1038/nrg.2016.112
- 734 Bonev, B., Cohen, N. M., Szabo, Q., Fritsch, L., Papadopoulos, G. L., Lubling, Y., et al. (2017). Multiscale
735 3D genome rewiring during mouse neural development. *Cell* 171, 557–572.e24. doi:10.1016/j.cell.2017.
736 09.043
- 737 Bonora, G., Plath, K., and Denholtz, M. (2014). A mechanistic link between gene regulation and genome
738 architecture in mammalian development. *Current Opinion in Genetics & Development* 27, 92–101.
739 doi:10.1016/j.gde.2014.05.002
- 740 Boya, R., Yadavalli, A. D., Nikhat, S., Kurukuti, S., Palakodeti, D., and Pongubala, J. M. (2017).
741 Developmentally regulated higher-order chromatin interactions orchestrate B cell fate commitment.
742 *Nucleic Acids Research* 45, 11070–11087. doi:10.1093/nar/gkx722
- 743 Branco, M. R. and Pombo, A. (2006). Intermingling of chromosome territories in interphase suggests role
744 in translocations and transcription-dependent associations. *PLoS Biology* 4, e138. doi:10.1371/journal.
745 pbio.0040138
- 746 Cremer, T. and Cremer, C. (2001). Chromosome territories, nuclear architecture and gene regulation in
747 mammalian cells. *Nature reviews genetics* 2, 292–301
- 748 Cremer, T., Cremer, M., Dietzel, S., Müller, S., Solovei, I., and Fakan, S. (2006). Chromosome territories—a
749 functional nuclear landscape. *Current opinion in cell biology* 18, 307–316

- 750 Cubeñas Potts, C. and Corces, V. G. (2015). Topologically associating domains: an invariant framework or
751 a dynamic scaffold? *Nucleus* 6, 430–434. doi:10.1080/19491034.2015.1096467
- 752 Dali, R. and Blanchette, M. (2017). A critical assessment of topologically associating domain prediction
753 tools. *Nucleic Acid Research* 45, 2994–3005. doi:10.1093/nar/gkx145
- 754 Darbellay, B., Arnaudeau, S., Ceroni, D., Bader, C. R., König, S., and Bernheim, L. (2010). Human muscle
755 economy myoblast differentiation and excitation-contraction coupling use the same molecular partners,
756 *stim1* and *stim2*. *Journal of Biological Chemistry* 285, 22437–22447
- 757 Davies, J. O., Oudelaar, A. M., Higgs, D. R., and Hughes, J. R. (2017). How best to identify chromosomal
758 interactions: a comparison of approaches. *Nature Methods* 14, 125–134. doi:10.1038/nmeth.4146
- 759 Dekker, J., Rippe, K., Dekker, M., and Kleckner, N. (2002). Capturing chromosome conformation. *Science*
760 295, 1306–1311. doi:10.1126/science.1067799
- 761 Dixon, J. R., Jung, I., Selvaraj, S., Shen, Y., Antosiewicz-Bourget, J. E., Lee, A. Y., et al. (2015).
762 Chromatin architecture reorganization during stem cell differentiation. *Nature* 518, 331–336. doi:10.
763 1038/nature14222
- 764 Dixon, J. R., Selvaraj, S., Yue, F., Kim, A., Li, Y., Shen, Y., et al. (2012). Topological domains in
765 mammalian genomes identified by analysis of chromatin interactions. *Nature* 485, 376–380. doi:10.
766 1038/nature11082
- 767 Doynova, M. D., Markworth, J. F., Cameron-Smith, D., Vickers, M. H., and O’Sullivan, J. M. (2017).
768 Linkages between changes in the 3D organization of the genome and transcription during myotube
769 differentiation in vitro. *Skeletal Muscle* 7, 1–14. doi:10.1186/s13395-017-0122-1
- 770 Durand, N. C., Shamim, M. S., Machol, I., Rao, S. S., Huntley, M. H., Lander, E. S., et al. (2016). Juicer
771 provides a one-click system for analyzing loop-resolution Hi-C experiments. *Cell Systems* 3, 95–98.
772 doi:10.1016/j.cels.2016.07.002
- 773 Eres, I. E. and Gilad, Y. (2020). A TAD skeptic: is 3D genome topology conserved? *Trends in Genetics* 37,
774 216–223. doi:10.1016/j.tig.2020.10.009
- 775 Feodorova, Y., Falk, M., Mirny, L. A., and Solovei, I. (2020). Viewing nuclear architecture through the
776 eyes of nocturnal mammals. *Trends in cell biology* 30, 276–289
- 777 Finn, E. H., Pegoraro, G., Brandao, H. B., Valton, A.-L., Oomen, M. E., Dekker, J., et al. (2019).
778 Extensive heterogeneity and intrinsic variation in spatial genome organization. *Cell* 176, 1502–1515.
779 doi:10.1016/j.cell.2019.01.020
- 780 Foissac, S., Djebali, S., Munyard, K., Vialaneix, N., Rau, A., Muret, K., et al. (2019). Multi-species
781 annotation of transcriptome and chromatin structure in domesticated animals. *BMC Biology* 17, 108.
782 doi:10.1186/s12915-019-0726-5
- 783 Foxcroft, G., Dixon, W., Novak, S., Putman, C., Town, S., and Vinsky, M. (2006). The biological basis
784 for prenatal programming of postnatal performance in pigs. *Journal of Animal Science* 84, E105–E112.
785 doi:10.2527/2006.8413_supplE105x
- 786 Fraser, J., Ferrai, C., Chiariello, A. M., Schueler, M., Rito, T., Laudanno, G., et al. (2015). Hierarchical
787 folding and reorganization of chromosomes are linked to transcriptional changes in cellular differentiation.
788 *Molecular Systems Biology* 11, 852. doi:10.15252/msb.20156492
- 789 Gibcus, J. H. and Dekker, J. (2013). The hierarchy of the 3D genome. *Molecular Cell* 49, 773–782.
790 doi:10.1016/j.molcel.2013.02.011
- 791 Giuffra, E., Tuggle, C. K., and FAANG Consortium (2019). Functional Annotation of Animal Genomes
792 (FAANG): current achievements and roadmap. *Annual Review of Animal Biosciences* 7, 65–88. doi:10.
793 1146/annurev-animal-020518-114913

- 794 Grant, C. E., Bailey, T. L., and Noble, W. S. (2011). FIMO: scanning for occurrences of a given motif.
795 *Bioinformatics* 27, 1017–1018. doi:10.1093/bioinformatics/btr064
- 796 Guarnieri, S., Morabito, C., Paolini, C., Boncompagni, S., Pilla, R., Fanò-Illic, G., et al. (2013). Growth
797 associated protein 43 is expressed in skeletal muscle fibers and is localized in proximity of mitochondria
798 and calcium release units. *PLoS One* 8, e53267
- 799 Guidi, M., Ruault, M., Marbouty, M., Loïodice, I., Cournac, A., Billaudeau, C., et al. (2015). Spatial
800 reorganization of telomeres in long-lived quiescent cells. *Genome Biology* 16, 206. doi:10.1186/
801 s13059-015-0766-2
- 802 Harada, A., Mallappa, C., Okada, S., Butler, J. T., Baker, S. P., Lawrence, J. B., et al. (2015). Spatial
803 re-organization of myogenic regulatory sequences temporally controls gene expression. *Nucleic Acids*
804 *Research* 43, 2008–2021. doi:10.1093/nar/gkv046
- 805 Harewood, L., Kishore, K., Eldridge, M. D., Wingett, S., Pearson, D., Schoenfelder, S., et al. (2017). Hi-C
806 as a tool for precise detection and characterisation of chromosomal rearrangements and copy number
807 variation in human tumours. *Genome Biology* 18, 125. doi:10.1186/s13059-017-1253-8
- 808 He, M., Li, Y., Tang, Q., Li, D., Jin, L., Tian, S., et al. (2018). Genome-wide chromatin structure
809 changes during adipogenesis and myogenesis. *International Journal of Biological Sciences* 14, 1571.
810 doi:10.7150/ijbs.25328
- 811 Hozé, N., Ruault, M., Amoruso, C., Taddei, A., and Holcman, D. (2013). Spatial telomere organization and
812 clustering in yeast *saccharomyces cerevisiae* nucleus is generated by a random dynamics of aggregation–
813 dissociation. *Molecular Biology of the Cell* 24, 1791–1800. doi:10.1091/mbc.E13-01-0031
- 814 Iannuccelli, E., Mompert, F., Gellin, J., Lahbib-Mansais, Y., Yerle, M., and Boudier, T. (2010).
815 NEMO: a tool for analyzing gene and chromosome territory distributions from 3D-FISH experiments.
816 *Bioinformatics* 26, 696–697. doi:10.1093/bioinformatics/btq013
- 817 Imakaev, M., Fudenberg, G., McCord, R. P., Naumova, N., Goloborodko, A., Lajoie, B. R., et al. (2012).
818 Iterative correction of Hi-C data reveals hallmarks of chromosome organization. *Nature Methods* 9,
819 999–1003. doi:10.1038/nmeth.2148
- 820 Lahbib-Mansais, Y., Barasc, H., Marti-Marimon, M., Mompert, F., Iannuccelli, E., Robelin, D., et al.
821 (2016). Expressed alleles of imprinted IGF2, DLK1 and MEG3 colocalize in 3D-preserved nuclei of
822 porcine fetal cells. *BMC Cell Biology* 17, 1–15. doi:10.1186/s12860-016-0113-9
- 823 Langmead, B. and Salzberg, S. L. (2012). Fast gapped-read alignment with Bowtie 2. *Nature Methods* 9,
824 357–359. doi:10.1038/nmeth.1923
- 825 Lazar-Stefanita, L., Scolari, V. F., Mercy, G., Muller, H., Guérin, T. M., Thierry, A., et al. (2017). Cohesins
826 and condensins orchestrate the 4D dynamics of yeast chromosomes during the cell cycle. *The EMBO*
827 *Journal* 36, 2684–2697. doi:10.15252/embj.201797342
- 828 Lefort, G., Servien, R., Quesnel, H., Billon, Y., Canario, L., Iannuccelli, N., et al. (2020). The maturity
829 in fetal pigs using a multi-fluid metabolomic approach. *Scientific Report* 10, 19912. doi:10.1038/
830 s41598-020-76709-8
- 831 Lieberman-Aiden, E., Van Berkum, N. L., Williams, L., Imakaev, M., Ragozy, T., Telling, A., et al. (2009).
832 Comprehensive mapping of long-range interactions reveals folding principles of the human genome.
833 *Science* 326, 289–293. doi:10.1126/science.1181369
- 834 Lin, Y. C., Benner, C., Mansson, R., Heinz, S., Miyazaki, K., Miyazaki, M., et al. (2012). Global changes
835 in the nuclear positioning of genes and intra- and interdomain genomic interactions that orchestrate B
836 cell fate. *Nature Immunology* 13, 1196–1204. doi:10.1038/ni.2432
- 837 Liu, Y., Zhou, J., and White, K. P. (2014). RNA-seq differential expression studies: more sequence or more
838 replication? *Bioinformatics* 30, 301–304

- 839 Long, H. K., Prescott, S. L., and Wysocka, J. (2016). Ever-changing landscapes: transcriptional enhancers
840 in development and evolution. *Cell* 167, 1170–1187. doi:10.1016/j.cell.2016.09.018
- 841 Lun, A. T. and Smyth, G. K. (2015). diffHic: a Bioconductor package to detect differential genomic
842 interactions in Hi-C data. *BMC Bioinformatics* 16, 258. doi:10.1186/s12859-015-0683-0
- 843 Lun, A. T. and Smyth, G. K. (2016). csaw: a Bioconductor package for differential binding analysis of
844 ChIP-seq data using sliding windows. *Nucleic Acids Research* 44, e45. doi:10.1093/nar/gkv1191
- 845 Lunney, J. K. (2007). Advances in swine biomedical model genomics. *International Journal of Biological
846 Sciences* 3, 179–184
- 847 Lupiáñez, D. G., Kraft, K., Heinrich, V., Krawitz, P., Brancati, F., Klopocki, E., et al. (2015). Disruptions
848 of topological chromatin domains cause pathogenic rewiring of gene-enhancer interactions. *Cell* 161,
849 1012–1025. doi:10.1016/j.cell.2015.04.004
- 850 Marti-Marimon, M., Vialaneix, N., Voillet, V., Yerle-Bouissou, M., Lahbib-Mansais, Y., and Liaubet, L.
851 (2018). A new approach of gene co-expression network inference reveals significant biological processes
852 involved in porcine muscle development in late gestation. *Scientific Report* 8, 10150. doi:10.1038/
853 s41598-018-28173-8
- 854 Mathelier, A., Fornes, O., Arenillas, D. J., Chen, C.-y., Denay, G., Lee, J., et al. (2016). JASPAR 2016: a
855 major expansion and update of the open-access database of transcription factor binding profiles. *Nucleic
856 Acids Research* 44, D110–D115. doi:10.1093/nar/gkv1176
- 857 McCarthy, D. J., Chen, Y., and Smyth, G. K. (2012). Differential expression analysis of multifactor
858 RNA-Seq experiments with respect to biological variation. *Nucleic Acids Research* 40, 4288–4297.
859 doi:10.1093/nar/gks042
- 860 McCord, R. P., Kaplan, N., and Giorgetti, L. (2020). Chromosome conformation capture and beyond:
861 toward an integrative view of chromosome structure and function. *Molecular cell* 77, 688–708
- 862 Meurens, F., Summerfield, A., Nauwynck, H., Saif, L., and Gerds, V. (2012). The pig: a model for human
863 infectious diseases. *Trends in Microbiology* 20, 50–57. doi:10.1016/j.tim.2011.11.002
- 864 Molenaar, C., Wiesmeijer, K., Verwoerd, N. P., Khazen, S., Eils, R., Tanke, H. J., et al. (2003). Visualizing
865 telomere dynamics in living mammalian cells using PNA probes. *The EMBO Journal* 22, 6631–6641.
866 doi:10.1093/emboj/cdg633
- 867 Mompert, F., Robelin, D., Delcros, C., and Yerle-Bouissou, M. (2013). 3d organization of telomeres
868 in porcine neutrophils and analysis of LPS-activation effect. *BMC Cell Biology* 14, 30. doi:10.1186/
869 1471-2121-14-30
- 870 Nagano, T., Lubling, Y., Stevens, T. J., Schoenfelder, S., Yaffe, E., Dean, W., et al. (2013). Single-cell Hi-C
871 reveals cell-to-cell variability in chromosome structure. *Nature* 502, 59–64. doi:10.1038/nature12593
- 872 Nagele, R. G., Velasco, A. Q., Anderson, W. J., McMahon, D. J., Thomson, Z., Fazekas, J., et al. (2001).
873 Telomere associations in interphase nuclei: possible role in maintenance of interphase chromosome
874 topology. *Journal of Cell Science* 114, 377–388
- 875 Nora, E. P., Lajoie, B. R., Schulz, E. G., Giorgetti, L., Okamoto, I., Servant, N., et al. (2012). Spatial
876 partitioning of the regulatory landscape of the X-inactivation centre. *Nature* 485, 381–385. doi:10.1038/
877 nature11049
- 878 Piórkowska, K., Tyra, M., Ropka-Molik, K., and Podbielska, A. (2017). Evolution of peroxisomal
879 trans-2-enoyl-coa reductase (pecr) as candidate gene for meat quality. *Livestock Science* 201, 85–91
- 880 Quinlan, A. R. (2014). BEDTools: the Swiss-army tool for genome feature analysis. *Current Protocols in
881 Bioinformatics* 47, 11.12.1–34. doi:10.1002/0471250953.bi1112s47
- 882 Ramani, V., Deng, X., Qiu, R., Gunderson, K. L., Steemers, F. J., Disteche, C. M., et al. (2017). Massively
883 multiplex single-cell Hi-C. *Nature Methods* 14, 263–266. doi:10.1038/nmeth.4155

- 884 Rao, S. S., Huntley, M. H., Durand, N. C., Stamenova, E. K., Bochkov, I. D., Robinson, J. T., et al. (2014).
885 A 3D map of the human genome at kilobase resolution reveals principle of chromatin looping. *Cell* 159,
886 1665–1680. doi:10.1016/j.cell.2014.11.021|
- 887 Rapaport, F., Khanin, R., Liang, Y., Pirun, M., Krek, A., Zumbo, P., et al. (2013). Comprehensive
888 evaluation of differential gene expression analysis methods for rna-seq data. *Genome biology* 14, 1–13
- 889 Rehfeldt, C., Fiedler, I., Dietl, G., and Ender, K. (2000). Myogenesis and postnatal skeletal muscle
890 cell growth as influenced by selection. *Livestock Production Science* 66, 177–188. doi:10.1016/
891 S0301-6226(00)00225-6
- 892 Rehfeldt, C. and Kuhn, G. (2006). Consequences of birth weight for postnatal growth performance
893 and carcass quality in pigs as related to myogenesis. *Journal of Animal Science* 84, E113–E123.
894 doi:10.2527/2006.8413_supplE113x
- 895 Robin, J. D., Ludlow, A. T., Batten, K., Magdinier, F., Stadler, G., Wagner, K. R., et al. (2014). Telomere
896 position effect: regulation of gene expression with progressive telomere shortening over long distances.
897 *Genes & Development* 28, 2464–2476. doi:10.1101/gad.251041.114
- 898 Robinson, M. D., McCarthy, D. J., and Smyth, G. K. (2010). edgeR: a Bioconductor package for
899 differential expression analysis of digital gene expression data. *Bioinformatics* 26, 139–140. doi:10.
900 1093/bioinformatics/btp616
- 901 Rudan, M. V., Barrington, C., Henderson, S., Ernst, C., Odom, D. T., Tanay, A., et al. (2015). Comparative
902 hi-c reveals that ctcf underlies evolution of chromosomal domain architecture. *Cell reports* 10, 1297–
903 1309
- 904 Sauerwald, N., Singhal, A., and Kingsford, C. (2020). Analysis of the structural variability of topologically
905 associated domains as revealed by Hi-C. *NAR Genomics and Bioinformatics* 2, lqz008. doi:10.1093/
906 nargab/lqz008
- 907 Schmitt, A. D., Hu, M., Jung, I., Xu, Z., Qiu, Y., Tan, C. L., et al. (2016). A compendium of chromatin
908 contact maps reveals spatially active regions in the human genome. *Cell Reports* 17, 2042–2059.
909 doi:10.1016/j.celrep.2016.10.061
- 910 Servant, N., Lajoie, B. R., Nora, E. P., Giorgetti, L., Chen, C.-J., Heard, E., et al. (2012). HiTC: exploration
911 of high-throughput ‘C’ experiments. *Bioinformatics* 28, 2843–2844. doi:10.1093/bioinformatics/bts521
- 912 Servant, N., Varoquaux, N., Lajoie, B. R., Viara, E., Chen, C.-J., Vert, J.-P., et al. (2015). HiC-Pro:
913 an optimized and flexible pipeline for Hi-C data processing. *Genome Biology* 16, 259. doi:10.1186/
914 s13059-015-0831-x
- 915 Sexton, T., Yaffe, E., Kenigsberg, E., Bantignies, F., Leblanc, B., Hoichman, M., et al. (2012). Three-
916 dimensional folding and functional organization principles of the Drosophila genome. *Cell* 148, 458–472.
917 doi:10.1016/j.cell.2012.01.010
- 918 Solov’eva, L., Svetlova, M., Bodinski, D., and Zalensky, A. O. (2004). Nature of telomere dimers
919 and chromosome looping in human spermatozoa. *Chromosome Research* 12, 817–823. doi:10.1007/
920 s10577-005-5513-1
- 921 Stevens, T. J., Lando, D., Basu, S., Atkinson, L. P., Cao, Y., Lee, S. F., et al. (2017). 3D structures
922 of individual mammalian genomes studied by single-cell Hi-C. *Nature* 544, 59–64. doi:10.1038/
923 nature21429
- 924 Tan, L., Xing, D., Chang, C.-H., Li, H., and Xie, X. S. (2018). Three-dimensional genome structures of
925 single diploid human cells. *Science* 361, 924–928. doi:10.1126/science.aat5641
- 926 Vietri Rudan, M., Barrington, C., Henderson, S., Ernst, C., Odom, D. T., Tanay, A., et al. (2015).
927 Comparative Hi-C reveals that CTCF underlies evolution of chromosomal domain architecture. *Cell*
928 *Reports* 10, 1297–1309. doi:10.1016/j.celrep.2015.02.004

- 929 Voillet, V., San Cristobal, M., Pèrè, M.-C., Billon, Y., Canario, L., Liaubet, L., et al. (2018). Integrated
930 analysis of proteomic and transcriptomic data highlights late fetal muscle maturation process. *Molecular*
931 *& Cellular Proteomics* 17, 672–693. doi:10.1074/mcp.M116.066357
- 932 Voillet, V., SanCristobal, M., Lippi, Y., Martin, P. G., Iannuccelli, N., Lascor, C., et al. (2014). Muscle
933 transcriptomic investigation of late fetal development identifies candidate genes for piglet maturity. *BMC*
934 *Genomics* 15, 797. doi:10.1186/1471-2164-15-797
- 935 Wang, X., Kam, Z., Carlton, P. M., Xu, L., Sedat, J. W., and Blackburn, E. H. (2008). Rapid telomere
936 motions in live human cells analyzed by highly time-resolved microscopy. *Epigenetics & Chromatin* 1,
937 4. doi:10.1186/1756-8935-1-4
- 938 Won, H., de La Torre-Ubieta, L., Stein, J. L., Parikshak, N. N., Huang, J., Opland, C. K., et al. (2016).
939 Chromosome conformation elucidates regulatory relationships in developing human brain. *Nature* 538,
940 523–527. doi:10.1038/nature19847
- 941 Yaffe, E. and Tanay, A. (2011). Probabilistic modeling of Hi-C contact maps eliminates systematic biases
942 to characterize global chromosomal architecture. *Nature Genetics* 43, 1059–1065. doi:10.1038/ng.947
- 943 Yamamoto, A. (2014). Gathering up meiotic telomeres: a novel function of the microtubule-organizing
944 center. *Cellular and Molecular Life Sciences* 71, 2119–2134. doi:10.1007/s00018-013-1548-1
- 945 Yang, T., Zhang, F., Yardimci, G. G., Song, F., Hardison, R. C., Noble, W. S., et al. (2017). HiCRep:
946 assessing the reproducibility of Hi-C data using a stratum-adjusted correlation coefficient. *Genome*
947 *Research* 27, 1939–1949. doi:10.1101/gr.220640.117
- 948 Yerle-Bouissou, M., Mompert, F., Iannuccelli, E., Robelin, D., Jauneau, A., Lahbib-Mansais, Y., et al.
949 (2009). Nuclear architecture of resting and LPS-stimulated porcine neutrophils by 3D FISH. *Chromosome*
950 *Research* 17, 847–862. doi:10.1007/s10577-009-9074-6
- 951 Zhang, N., Mendieta-Esteban, J., Magli, A., Lilja, K. C., Perlingeiro, R. C., Marti-Renom, M. A., et al.
952 (2020). Muscle progenitor specification and myogenic differentiation are associated with changes in
953 chromatin topology. *Nature Communications* 11, 6222. doi:10.1038/s41467-020-19999-w
- 954 Zheng, H. and Xie, W. (2019). The role of 3d genome organization in development and cell differentiation.
955 *Nature Reviews Molecular Cell Biology* 20, 535–550. doi:10.1038/s41580-019-0132-4
- 956 Zufferey, M., Tavernari, D., Oricchio, E., and Ciriello, G. (2018). Comparison of computational methods
957 for the identification of topologically associating domains. *Genome Biology* 19, 217. doi:10.1186/
958 s13059-018-1596-9

TABLES

FIGURE CAPTIONS

Tested telomere interaction	Proportion of nuclei with interaction (total number of nuclei)	
	90 days of gestation	110 days of gestation
SSC9qter – SSC2pter	24% (100)	15% (100)
SSC9qter – SSC13qter	19% (99)	15% (100)
SSC9qter – SSC15qter	28% (100)	20% (97)

Table 1. Numbers and proportions of nuclei with an observed association between telomeres. Proportions of nuclei harboring the probed telomeric associations in muscle cells at 90 and 110 days of gestation: SSC2pter – SSC9qter, SSC13qter – SSC9qter and SSC15qter – SSC9qter. For each association, ~100 nuclei were analyzed. A higher percentage of association is observed at 90 days of gestation for the three tested associations.

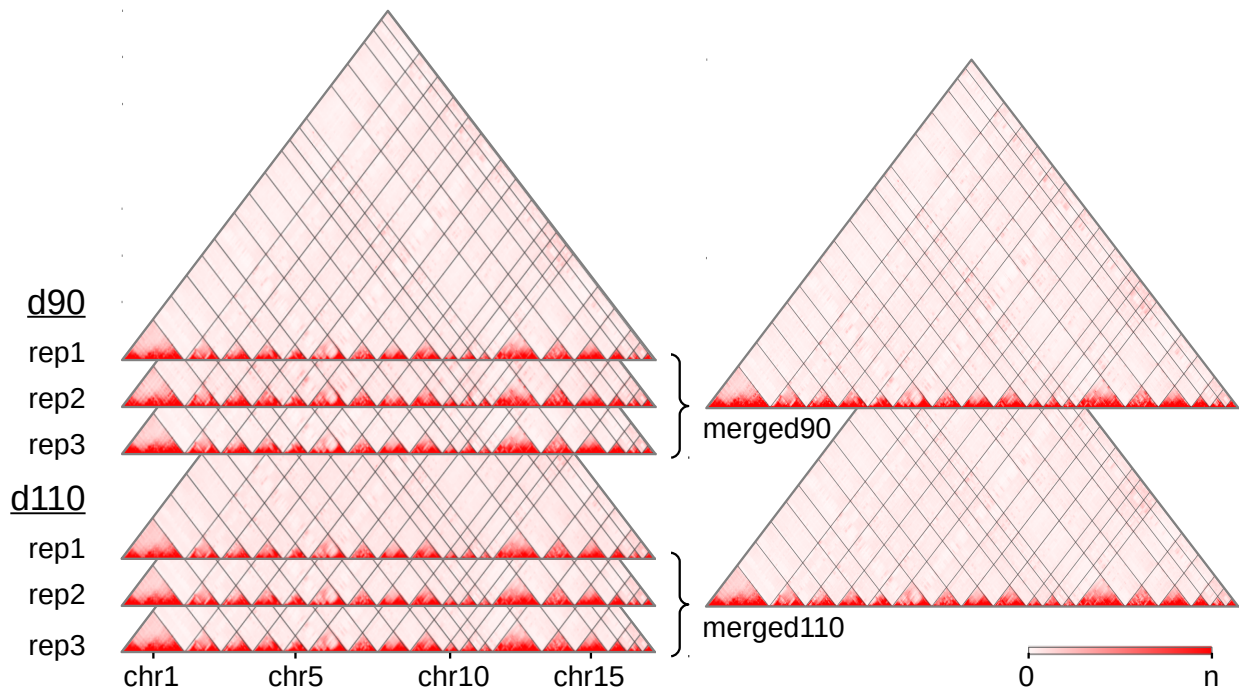


Figure 1. Hi-C interaction maps of the porcine genome in fetal muscle. Interaction matrices of three biological replicates from two experimental groups (90 and 110 days of gestation) were displayed with the Juicebox tool, before and after merging them by group. The color intensity indicates the number of interactions between pairs of genomic loci (x -axis, 500 Kb per bin). Since the color scale is generated for each matrix independently, the highest intensity corresponds to the following values of n : 16,103 (rep1), 13,257 (rep2) and 11,461 (rep3) for d90, 13,022 (rep1), 7,150 (rep2) and 16,070 (rep3) for d110, 43,029 for merged90 and 37,866 for merged110. As the *Sus scrofa* v11.1 assembly version contains 613 scaffolds, only the 18 assembled autosomes are displayed. See also Supplementary Table 2.

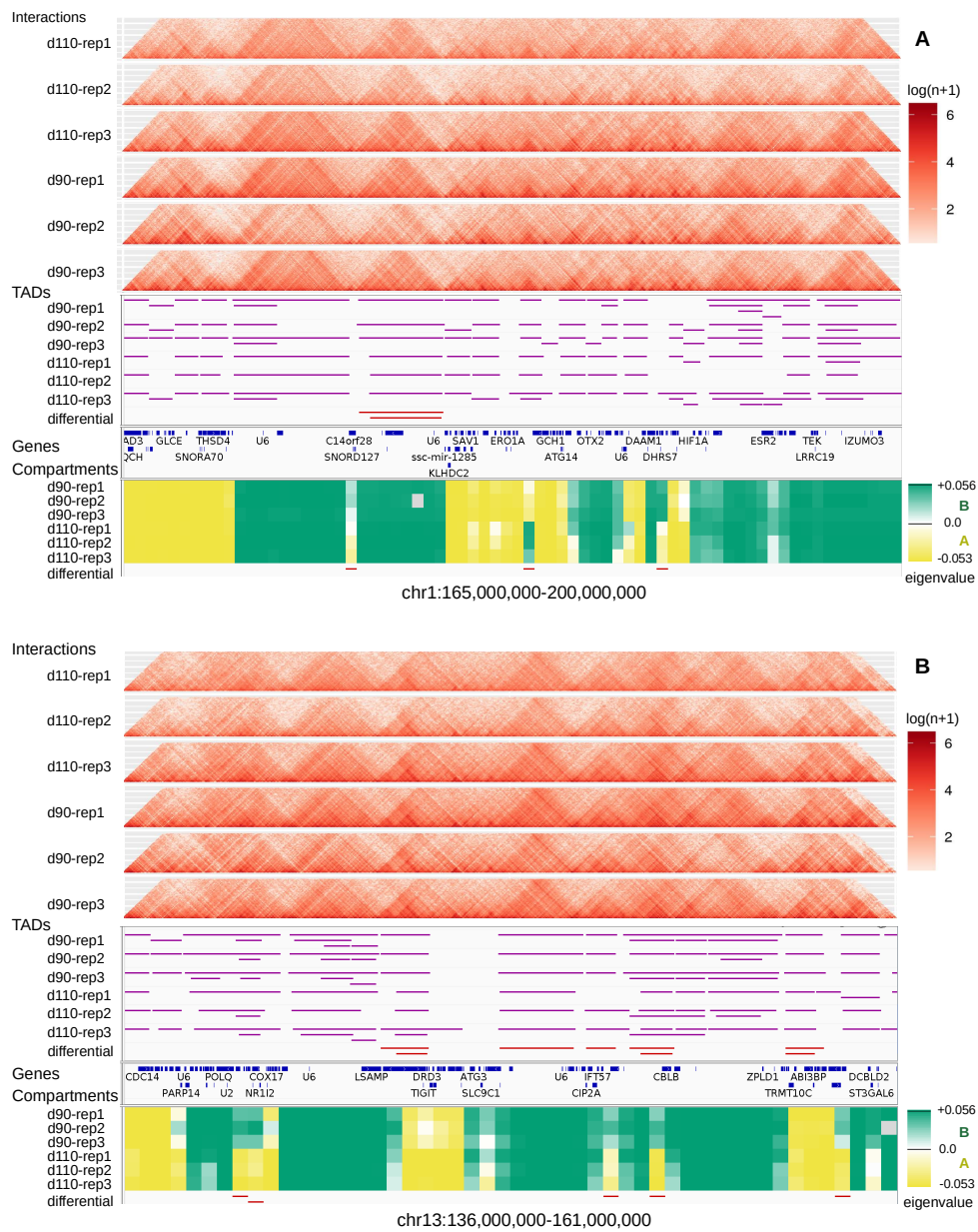


Figure 2. Landscape of topological features in the pig genome. Hi-C interaction maps (top, heatmaps), TADs (middle, horizontal purple lines), and genomic compartments (bottom, green/yellow eigenvalues for A/B compartments respectively) are displayed for the six samples at two loci of the pig genome: one on chromosome 1 (A) and one on chromosome 13 (B). Annotated genes are listed between TADs and compartments. The last track (at the bottom) shows regions with a consistent switch of compartment for all replicates (AAA → BBB or BBB → AAA).

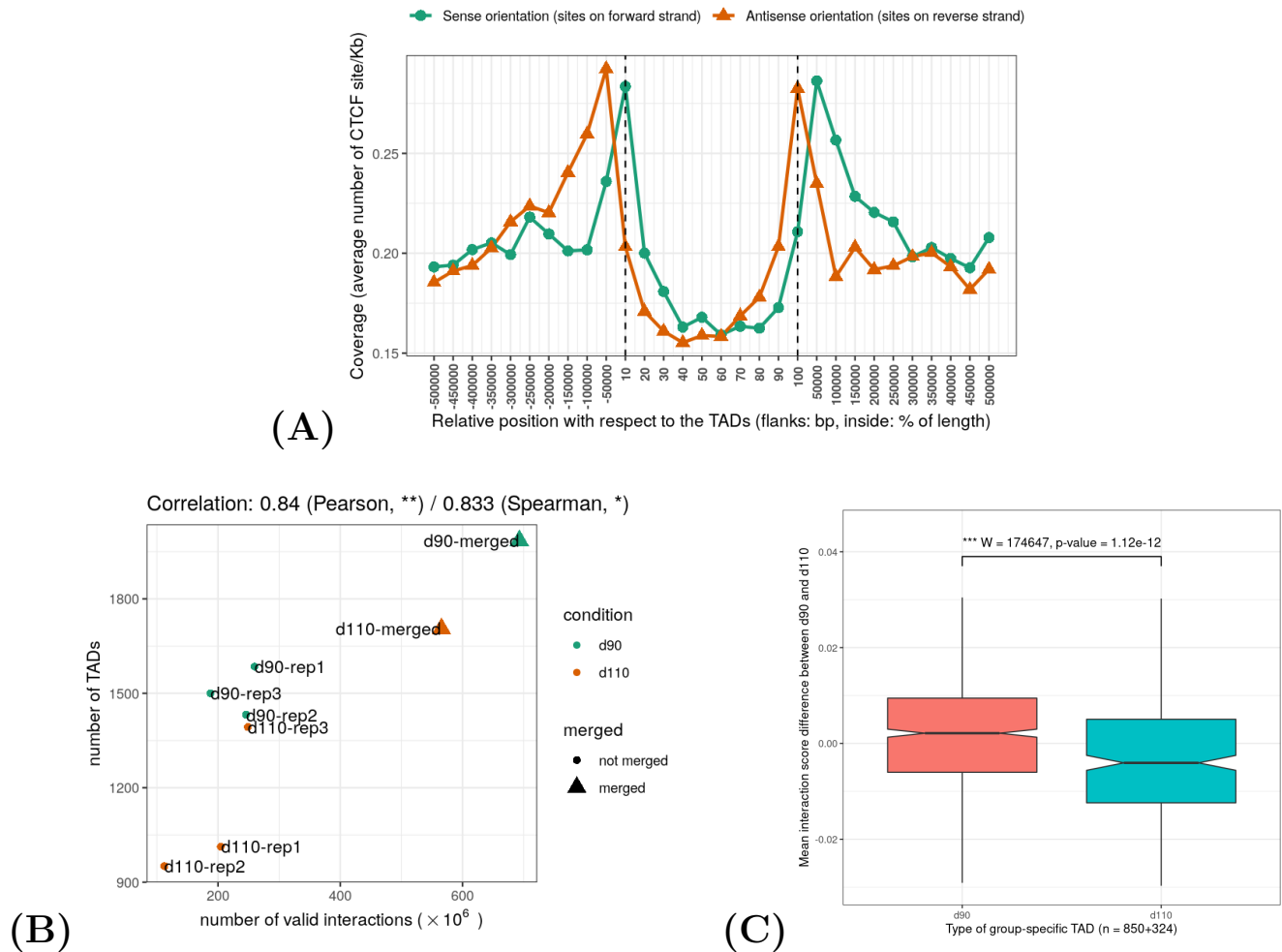


Figure 3. Characteristics of Topologically Associating Domains (TADs). (A) The genomic distribution of CTCF binding sites over TAD regions shows an accumulation of sites at the TAD boundaries in the expected inwards orientation, meaning forward and reverse sites respectively at the beginning and at the end of TADs. Flanking TADs explain the shifted peaks corresponding to sites in the outwards orientation. (B) Correlation between Hi-C matrix density (number of interactions) and number of predicted TADs. (C) Distributions of Interaction Score Differences between 90 and 110 days of gestation for boundaries of d90- and d110-specific TADs.

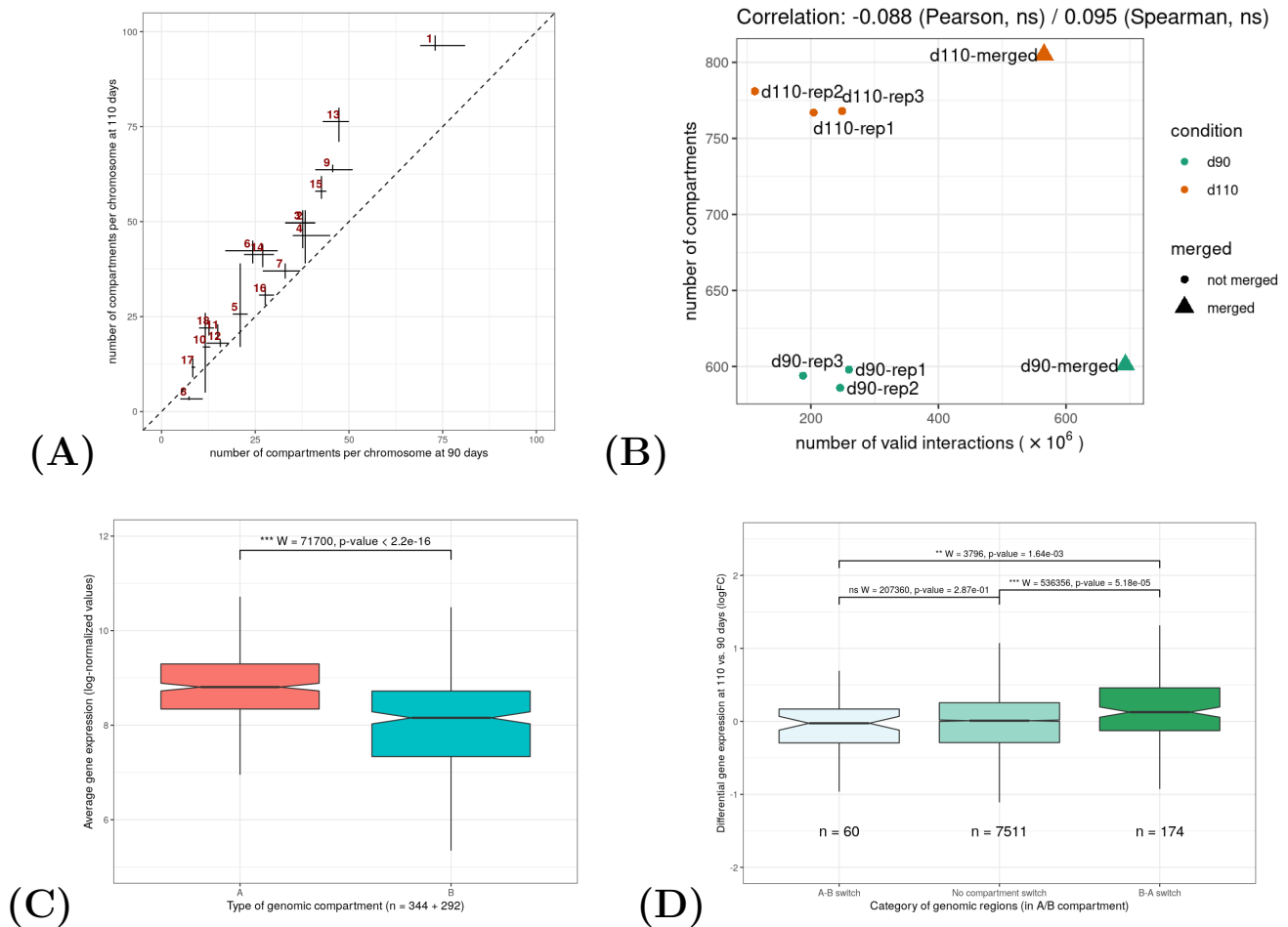


Figure 4. Features of A/B genomic compartments. (A) Average number of compartments per chromosome at 90 and 110 days of gestation. The dotted line indicates $y = x$. (B) Relation between the number of valid interactions in each matrix and the number of compartments. Unlike for TADs (Figure 3B), no impact was detected. (C) Average expression of genes in A vs. B compartments. Gene expression data were obtained from a previous study of fetal muscle samples at 90 and 110 days of gestation Voillet et al. (2014). (D) Distribution of differential expression values (logFC) for genes in genomic regions: (left) switching from an A compartment at 90 days to a B compartment at 110 days (A-B switch); (middle) showing no compartment switch; (right) switching from a B compartment at 90 days to an A compartment at 110 days (B-A switch). See also Figures S1 and S2.

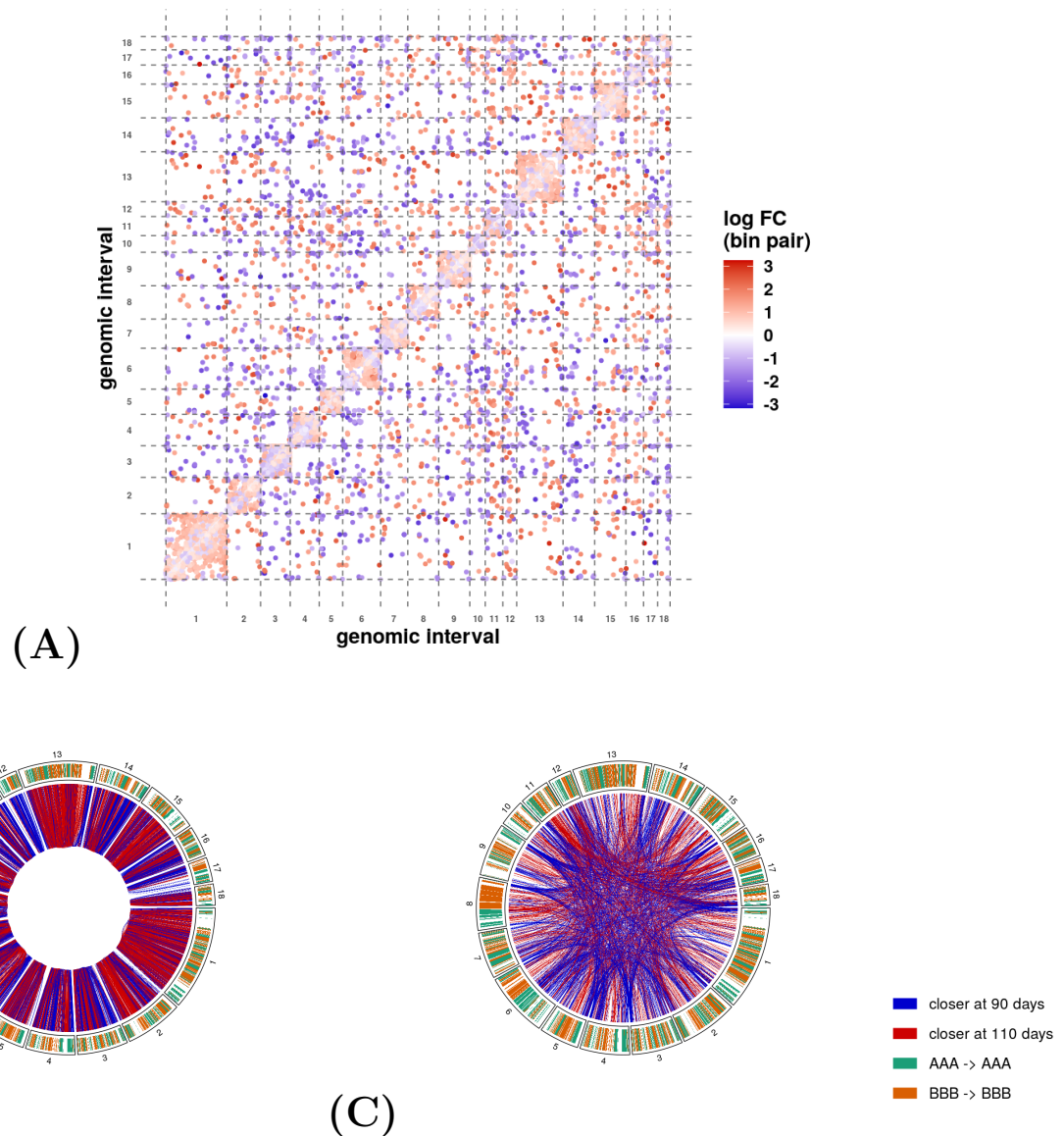


Figure 5. Pairs of genomic regions with differential interactions between 90 and 110 days of gestation. Results of the comparative analysis of the Hi-C matrices at 500 Kb resolution show differential interactions along the 18 assembled autosomes. (A) Differential interaction matrix. Each dot represents a pair of genomic interval with a significantly different interaction value and its associated log-fold change value (logFC, blue-white-red gradient scale). Positive values of logFC correspond to genomic regions closer at 110 days of gestation than at 90 days (red dots). Inversely, negative values indicate regions that were closer at 90 days (blue dots). Same colors are used to display *cis* (B) and *trans* (C) differential interactions as red (positive logFC) or blue (negative logFC) connections between genomic regions (outer circle). Chromosome inner color shows the genomic segmentation into A (turquoise) and B (orange) stable compartments. See also Figures S3 and S4.

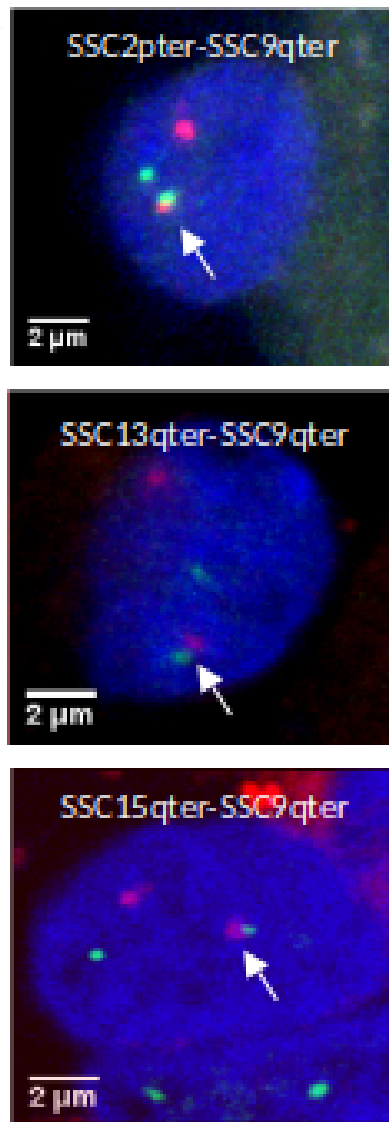


Figure 6. 3D DNA FISH validation of preferential associations of telomeres in muscle cells. 3D images illustrating telomeric associations (SSC2pter – SSC9qter), (SSC13qter – SSC9qter) and (SSC15qter – SSC9qter) at 90 days of gestation. Maximum intensity projections of confocal image stacks are shown. SSC2p, SSC13q and SSC15q telomeres are labelled in green (Alexa 488) and SSC9qter telomere probe in red (Alexa 568). Nucleus DNA was counterstained in blue with DAPI.